ELSEVIER

Journal of Fluids and Structures 24 (2008) 855–882

JOURNAL OF FLUIDS AND STRUCTURES

www.elsevier.com/locate/jfs

Experimental investigation of a confined flow downstream of a circular cylinder centred between two parallel walls

F. Rehimi[a,b], F. Aloui[a,*], S. Ben Nasrallah[b], L. Doubliez[a], J. Legrand[c]

[a]*Université de Nantes, Faculté des Sciences et des Techniques, Laboratoire GEPEA-CNRS-UMR 6144,2, rue de la Houssinière BP 92208–44322 Nantes Cedex 03, France*

[b]*Laboratoire LESTE, Université de Monastir, École Nationale d'Ingénieurs de Monastir, Avenue Ibn El Jazzar 5019, Monastir, Tunisie*

[c]*Laboratoire GEPEA-CNRS-UMR 6144, Université de Nantes, CRTT, BP 406 44602 Saint-Nazaire Cedex, France*

Received 21 February 2006; accepted 8 December 2007
Available online 8 May 2008

Abstract

In this work, we present an experimental study of the wall confinement effect on the wake formation behind a circular cylinder of diameter $d_c = 10$ mm and of length $L_c = 30d_c$. The experiments were performed in a water tunnel with the dimensions (length $= 300d_c$, height $= 3d_c$, span $L_c = 30d_c$). The confinement rate was $r = 1/3$ and the Reynolds number was in the range of 30–277. The experiments were done using 2-D PIV measurements. The first instability was delayed by the confinement and the von Kármán vortices characteristics are different from the unconfined case. Proper orthogonal decomposition (POD) of the flow was used for a filtering purpose and to extract the energetic contribution of the different modes. A low-order representation of the flow, constructed from the first pair of modes in the well-defined region of the flow, shows that von Kármán vortices are equivalent to vanishing progressive waves. Measurements done above the cylinder show the presence of 3-D span instabilities showing great similarities with "Mode A" and "Mode B" found in the unconfined case.

Keywords: von Kármán vortex shedding; Confined cylinder wake; POD decomposition; Coherent structures; Instability; PIV

1. Introduction

The study of the cylinder wakes in an infinite medium has a very important practical interest. In fact, the knowledge of the generation mechanism of the large eddies behind obstacles, their shedding frequencies and their different scales are very important in the design of structures exposed to fluid flows. We have restricted our attention to the range of Reynolds number where there exists a laminar von Kármán vortex street. Much work has been devoted to these kinds of flows. Williamson (1996) has given a review for unbounded flow past a circular cylinder, and many results were gathered by Zdravkovich (1997, 2003). The presence of walls near the cylinder leads to a blockage. The effects due to the confinement are more often studied numerically (Anagnostopoulos et al., 1996; Zovatto and Pedrizzetti, 2001; Carte et al., 1995a, b; Guerrouache, 2000; Sahin and Owens, 2004), but the experimental results are scarce (Chen et al., 1995; Coutanceau and Bouard, 1977).

*Corresponding author. Tel.: +33 2 51 12 55 07; fax: +33 2 51 12 55 05.
E-mail address: fethi.aloui@univ-nantes.fr (F. Aloui).

0889-9746/$ - see front matter © 2008 Elsevier Ltd. All rights reserved.
doi:10.1016/j.jfluidstructs.2007.12.011

Nomenclature

A	y-dependent complex vectors
$a^{(n)}$	POD temporal coefficient ($m\,s^{-1}$)
B	y-dependent complex vectors
$b_x^{(1)}$	y-dependent function
C	dimensionless coefficient
C_0	dimensionless coefficient
d_c	cylinder diameter (m)
D_v	flow rate in the channel ($m\,s^{-1}$)
E	integer part function
E_c	mean rotating kinetic energy ($m^2\,s^{-2}$)
Enst	spatial average Enstrophy of a vortex (s^{-2})
f_{St}	Strouhal frequency (Hz)
f_s	Shedding frequency (Hz)
$g_x^{(1)}$	spatial function
$g_y^{(1)}$	spatial function
G	spatial dependent function
j	complex unit ($j^2=-1$)
$\tilde{k}$	complex wavenumber
k'	wavenumber (m^{-1})
k''	damping coefficient (m^{-1})
L_F	formation length (m)
L_r	recirculation region (m)
l	y-dependent function
$p_x^{(1)}$	x-dependent function
Q	Q criterion (s^{-2})
$q_x^{(1)}$	y-dependent function
$q_y^{(1)}$	y-dependent function
r	confinement ratio
$\Re$	temporal correlation tensor
Re	Reynolds number (dimensionless)
S	integration surface (m^2)
S_v	vortex area (m^{-2})
St	Strouhal number (dimensionless)
Sign	sign function
$\mathbf{U}$	velocity vector ($m\,s^{-1}$)
$\tilde{\mathbf{U}}$	velocity used in the Γ_2 criterion ($m\,s^{-1}$)
U_m	height-averaged velocity ($m\,s^{-1}$)
U_∞	free-stream velocity ($m\,s^{-1}$)
u_{rms}	axial root mean square velocity
$\mathbf{V}$	eigenvector of the correlation matrix
v_{rms}	normal root mean square velocity ($m\,s^{-1}$)
x, y, z	coordinate (m)
x_s	axial position of $(v_{rms})_{max}$ (m)
2D–2C–PIV	two component velocities obtained by PIV
∇	gradient operator

Greek letters

α, β	real coefficients
γ	gap parameter (dimensionless)
Γ	vortex circulation
Γ^*	dimensionless vortex circulation
Γ_2	for vortex center identification (dimensionless)
$\delta_{m,n}$	Kronecker symbol
Δ	gap (m)
λ	eigenvalues of POD decomposition
$\mathbf{\Psi}_1$	first complex mode
Λ	wavelength (m)
r, θ	polar coordinate (m, rd)
ν	kinematic viscosity ($m^2\,s^{-1}$)
$\mathbf{\Phi}$	POD modes
χ, ξ, ζ	phases
ω	vorticity (s^{-1})
Ω_s	Strouhal pulsation ($rd\,s^{-1}$)

Subscripts

ad	relative to the advection velocity of the vortex
c	critical
cl	centreline value
loc	local value
m	height-average
max	maximum
mean	temporal average velocity of measurements

Superscripts

~	average calculated from neighbouring points
*	dimensionless
e	estimated
gap	gap between cylinder and wall

The flow around a circular cylinder in an infinite medium is conditioned by the Reynolds number $Re = U_\infty d_c/\nu$ (where U_∞ is the free-stream velocity, d_c is the cylinder diameter, and ν is the kinematic viscosity). When $Re < 5$, the creeping is characterised by the preponderance of the viscous effects (Coutanceau and Defaye, 1991; Williamson, 1996). When $5 < Re < 47$, two steady recirculation regions are set up behind the cylinder. The size of the recirculation regions were well-defined by Coutanceau and Defaye (1991). For $Re \approx 47$, the wake becomes unstable, manifesting the appearance of a vortex street. The shedding frequency is generally presented in a dimensionless form by the Strouhal number, defined as $St = f_s d_c/U_\infty$. This instability is found to be a manifestation of a Hopf bifurcation (Provensal et al., 1987). When $47 \leqslant Re \leqslant 190$, the Strouhal number is an increasing function of Reynolds number, and several authors (Karniadakis and Triantafyllou, 1989; Williamson, 1996) tried to find universal expression for $St = f(Re)$. At $Re \approx 190$, occurs a first transition to three-dimensional (3-D) flow which is characterised by a discontinuity in the function $St = f(Re)$. At $Re \approx 260$, a second transition occurs which is also characterised by a discontinuity in $St = f(Re)$. Williamson (1996) and Brede et al. (1996) showed that the two discontinuities appearing in the relation $St = f(Re)$ for

$190 \leqslant Re \leqslant 260$ are a consequence of two spanwise instabilities known as modes A and B. Mode A appears at $Re \approx 190$, and is characterised by a spatial scale $\Lambda_A = 3 - 4d_c$. Mode B appears gradually after mode A, and is characterised by a spatial scale $\Lambda_B = 0.9d_c$ to $1d_c$. These instabilities can be highlighted by doing spatiotemporal cross-correlations in the spanwise direction of the cylinder wake.

In the case of a cylinder between parallel walls, two additional parameters control the dynamics of the cylinder wake. These latter are the gap parameter $\gamma = \Delta/d_c$ (Δ is the distance between the cylinder and the nearest wall), and the confinement ratio $r = d_c/H$ (H is the distance separating the two walls). The critical Reynolds number, which is about $Re_c \approx 47$ in absence of confinement, increases with the confinement ratio and also the shedding frequency. By decreasing the gap parameter, the von Kármán vortex street can be restricted to one row of vortices of the same sign (Zovatto and Pedrizzetti, 2001). For very small gap parameters, the investigations of Bearman and Zdravkovich (1978), Sumer et al. (1991), Lei et al. (1999), Price et al. (2002) have shown experimentally the suppression of the von Kármán vortex street. In the literature, few works investigated in the cylinder wake between parallel walls (Coutanceau and Bouard, 1977; Anagnostopoulos et al., 1996). These works, which are especially based on 2-D numerical simulations, have studied the effect of the confinement ratio and of the gap parameter on the aerodynamical coefficients (drag and lift) or on the Strouhal number. Braza et al. (2006) have presented both an experimental and numerical work for a confined cylinder at $Re \approx 140\,000$ and insisted on the fact that confined configurations allow direct comparisons with 3-D Navier–Stokes computations avoiding infinite (unbounded) conditions.

In this paper, an experimental investigation of a confined circular cylinder wake is presented. For this purpose, a cylinder of 10 mm diameter is placed in a channel with a rectangular cross-section of $300 \times 30\,mm^2$. The water channel span is about $30d_c$. The Reynolds number range studied is small, and the upstream flow is laminar with no upstream turbulence. The confinement ratio and the gap parameter are fixed in this study as $r = 1/3$ and $\gamma = 1$. Measurements in the cylinder wake were done using the particle image velocimetry (PIV) technique for the different flow regimes and in different sections. The main objective of this work is to study the influence of confinement on the different flow regimes and the reorganisation of the flow in the cylinder wake. It is essential also to add that such a case is more suitable for the validation of numerical simulations than the unconfined case. The choice of this configuration was guided by the numerical simulations of Carte et al. (1995a, b) and Guerrouache (2000) for $r = 1/3$ and $\gamma = 1$.

2. Experimental set-up and measurement techniques

2.1. Experimental set-up

The hydraulic tunnel made up of transparent plexiglas is shown in Fig. 1(a). The test-section measures 3.3 m in length, $2a = 0.3$ m in width and $2b = 0.03$ m in height (Fig. 1(b) and (c)). It is fed by a tank where the water level is maintained constant by an overflow. A cylinder of $d_c = 10^{-2}$ m in diameter is placed in the test-section perpendicularly to the mean flow direction at $L_b = 1.67$ m from the entry. The gap parameter is $\gamma = \Delta/d_c = 1$, where Δ is the distance between cylinder and the nearest wall, and the confinement ratio is $r = d_c/2b = 1/3$. The mean velocity flow in the channel section upstream the cylinder was in the range 0.2–1.85 cm s^{-1}.

2.2. Measurement techniques

The PIV system used for the determination of the velocity field was essentially composed of a CCD camera of 1600×1186 pixels resolution (Dantec Dynamics Flow Sense M2/E 8 bits) with a Nikon (60 mm) objective, a pulsed Nd-Yag 15 mJ Laser (New Wave Solo) and a "DANTEC" correlator. The whole system is driven by the "DANTEC" software "Flow Manager". The flow seeding was done by using 50 μm spherical polyamide particles. Three flow field areas (measurement positions in Fig. 2(c) and (d)) were studied. The first one at $z = 0$ with $0 \leqslant x \leqslant 8 \leqslant d_c$ and $-1.5d_c \leqslant y \leqslant 1.5d_c$, where x, y and z are respectively the axial, vertical and transverse coordinates (Fig. 1). The second area (position 2) was at $z = 0$ with $9d_c \leqslant x \leqslant 18d_c$ and $-1.5d_c \leqslant y \leqslant 1.5d_c$. The choice of the first two configurations was conditioned by the presence of screws used to assemble the body of the channel. The third area position (position 3 in Fig. 2(d)) was situated above the cylinder at $y = 1.25d_c$ with $0 \leqslant x \leqslant 20d_c$ and $-7d_c \leqslant z \leqslant 7d_c$. The aim of measurements in this third configuration is to detect any 3-D transition in the span direction of the flow.

For positions 1 and 2, the horizontal laser plane was reflected vertically at $z = 0$ using a 45° mirror. In these cases, the camera was placed directly in front of the lateral wall flow. The physical field of view in the position 1 of measurement was $81.73 \times 60.59\,mm^2$. A mask was applied to retain only 30 mm in the y-direction from 60.59 mm. In the position 2 of measurement, the camera field of view was $180.8 \times 60.59\,mm^2$ and by applying a mask, only 30 mm in the y-direction was retained. For measurements at position 3, the laser was displaced to be in the plane $y = 1.25d_c$ and the flow field is

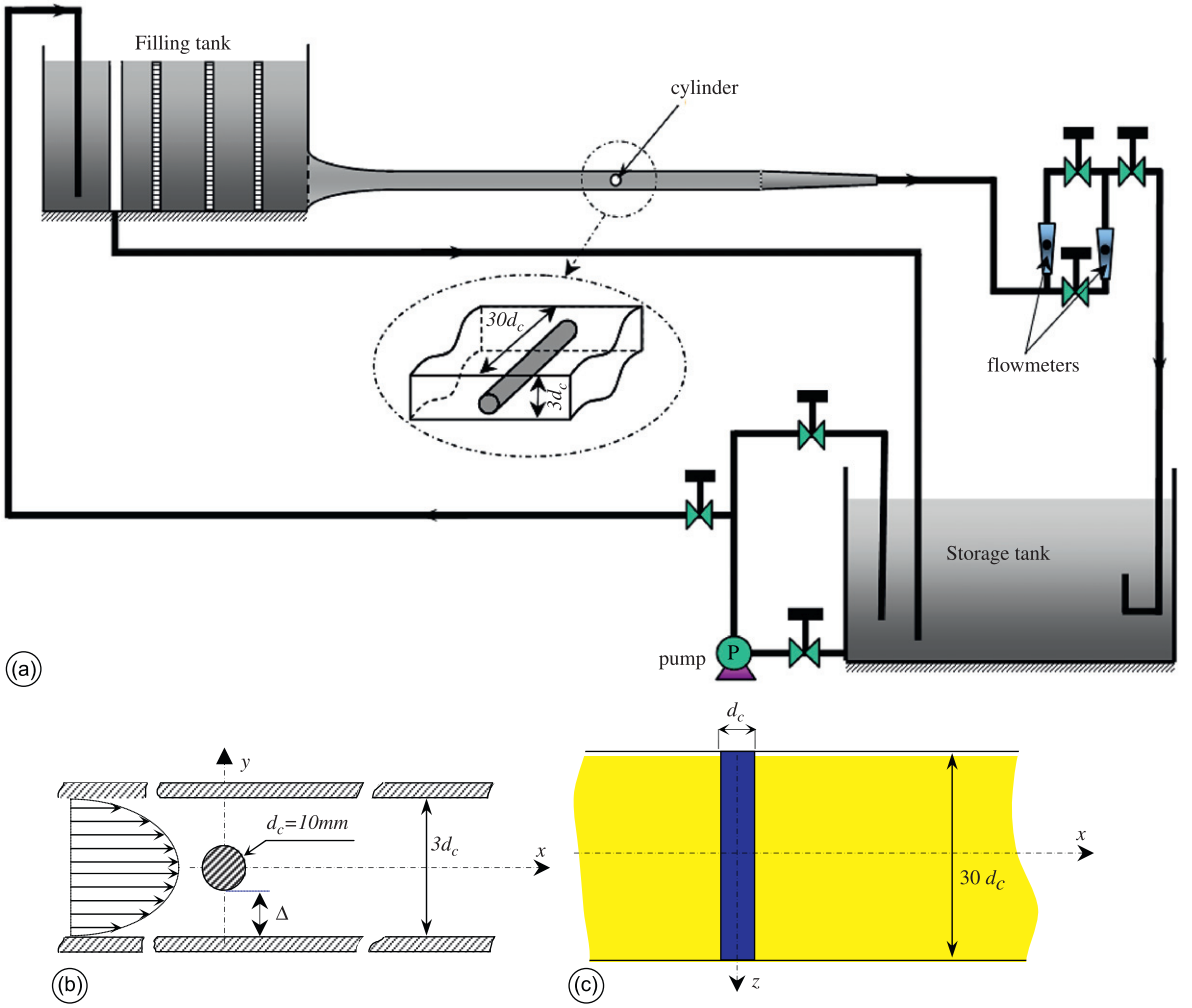

Fig. 1. Hydraulic channel: (a) schematic view of the setup; (b) face view; and (c) upper view.

reflected towards the camera by the mirror. All the fields of view used in this case were $201.51 \times 147.77\,\text{mm}^2$. For the measurements in configurations 1 and 2, the interrogation areas were 32×32 pixels. For measurements in the plane $y = 1.25d_c$, the interrogation areas were 16×16 pixels. An adaptative cross correlation was used with an overlap of 50%. For the measurements in positions 1 and 2, the spatial resolutions are respectively $\Delta x = \Delta y = 0.85\,\text{mm}$ and $\Delta x = \Delta y = 0.93\,\text{mm}$ at the same sampling frequency $f_e = 15\,\text{Hz}$ and for a duration of 20 s. For the third position measurement, we have $\Delta x = \Delta z = 1.1\,\text{mm}$ for the same frequency and the duration is identical to that of the first two configurations. Frequency analysis shows that the maximum shedding frequency for the flow range studied is about 1.4 Hz. As the acquisition frequency is $f_e = 15\,\text{Hz}$, the experiment is considered as time resolved.

3. Coherent structures detection and proper orthogonal decomposition (POD) decomposition of the flow

3.1. Coherent structures detection

Coherent structure interaction and the mechanism of generation and dissipation constitute a fundamental topic in fluid mechanics research, especially because they play an essential role in heat and mass transfer problems. The most debated questions with coherent structures include: how do we detect the centre of a vortex, how do we define its limits and how do we quantify its energy?

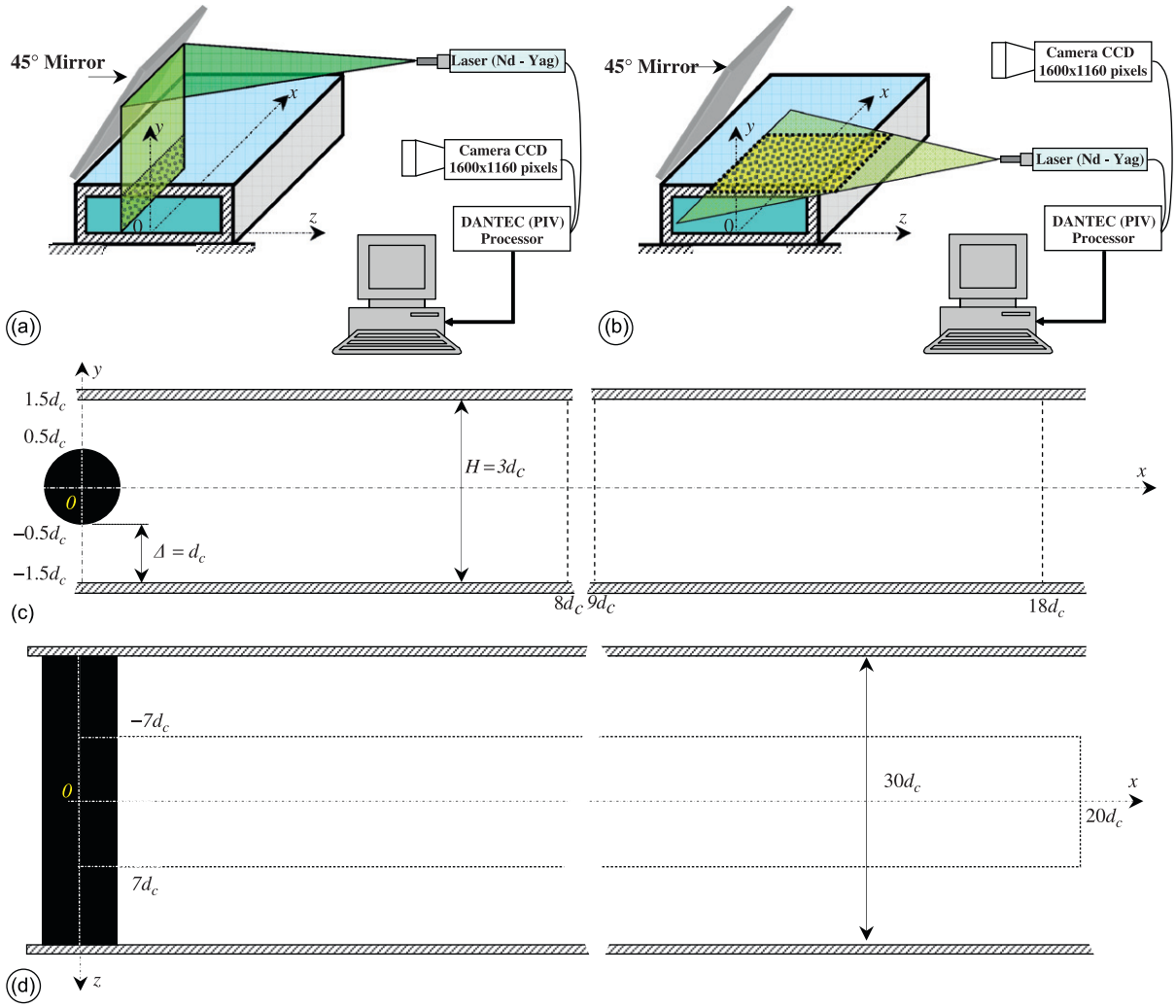

Fig. 2. PIV measurements positions: (a) 3-D view of the measurement configurations 1 and 2; (b) 3-D view of measurement position 3; (c) measurement positions 1 and 2; and (d) measurement position 3 (above the cylinder at $y = 2.75d_c$).

Many criteria are used in practice (Haller, 2005) and they are always deduced from the velocity gradient tensor. The vorticity magnitude is widely used to identify the coherent structures present in the flow. It is a Galilean invariant and is defined for a 2-D flow as follows:

$$\omega = \frac{1}{2}\left(\frac{\partial U_y}{\partial x} - \frac{\partial U_x}{\partial y}\right). \tag{1}$$

The use of vorticity magnitude is successful in free shear flows. In our case, the presence of shear at the upper and the lower wall deforms the vorticity patterns of the coherent structure.

An often used criterion for coherent structures detection is the second invariant of the velocity gradient tensor known under the name of the Q criterion. It was proposed by Hunt et al. (1988), and it is defined for a 2-D flow by the following relation:

$$Q = -\frac{1}{2}\left[\left(\frac{\partial U_x}{\partial x}\right)^2 + 2\left(\frac{\partial U_x}{\partial y}\right)\left(\frac{\partial U_y}{\partial x}\right) + \left(\frac{\partial U_y}{\partial y}\right)^2\right]. \tag{2}$$

The Q criterion can be interpreted as a balance between the rotation rate and the strain rate. This criterion allows to define the limit of a coherent structure from the positive values of Q. It is interesting to notice that this criterion is not affected by the local shear.

For a 2-D fluid flow, Graftieaux et al. (2001) have proposed two kinematic criteria, Γ_1 for the vortex centre identification and Γ_2 for a vortex core identification. As the Γ_1 criterion is not Galilean-invariant but Γ_2 is, we propose in this work to use the extremum of the Γ_2 criterion for the vortex centre identification. This criterion gives accurate results in the vortex center identification in comparison with the vorticity magnitude or the Q criterion and it is defined as follows:

$$\Gamma_2(P) = \frac{1}{S}\int_{M\in S} \frac{(\mathbf{PM} \wedge (\mathbf{U}(M) - \tilde{\mathbf{U}}(P))) \cdot \mathbf{e}_z}{\|\mathbf{PM}\| \cdot \left\|\mathbf{U}(M) - \tilde{\mathbf{U}}(P)\right\|} \,\mathrm{d}S, \tag{3}$$

where $\tilde{\mathbf{U}}(P) = (1/S)\int_{M'\in S} \mathbf{U}(M')\,\mathrm{d}S$, $\boldsymbol{e}_z$ is a unit vector perpendicular to the velocity map, P is the point where the criterion is calculated, and S is a local surface surrounding the point P. The local surface S can be chosen circular or rectangular. For a large S, the small scales in the flow are filtered, so S should be as small as possible. The size of S retained in our case is $S = 9\Delta x\,\Delta y$. In the case of vector map with moderate resolution, the maximum of Γ_2 is not a point but a quasi-circular region. Then, it is assumed that the vortex centre is defined by the maximum of Γ_2 and the minimum of $\mathbf{U}(x, y, t) - \mathbf{U}_{\mathrm{ad}}(t)$, where $\mathbf{U}_{\mathrm{ad}}(t)$ is the advection velocity of the vortex at the time t. The advection velocity $\mathbf{U}_{\mathrm{ad}}(t)$ is calculated in two steps. The first step consists in calculating an estimate $\mathbf{U}^e_{\mathrm{ad}}(t)$ of $\mathbf{U}_{\mathrm{ad}}(t)$ from the Γ_2 criterion. The value of $\mathbf{U}^e_{\mathrm{ad}}(t)$ is deduced from the vortex shifting between two successive velocity maps. After this, the vortex centre is estimated recurrently using the Γ_2 criterion and the minimum of $\mathbf{U}(x, y, t) - \mathbf{U}^e_{\mathrm{ad}}(t)$ until $\mathrm{U}^e_{\mathrm{ad}}(t)$ does not change.

3.2. POD decomposition of the flow

The calculation of the vorticity, enstrophy or velocity gradient tensor is based on the derivatives of the velocity field deduced from the PIV data. These measurements are generally noisy. By applying the derivatives, high noise frequencies are amplified. For this reason, filtering was applied. The filter has to take into consideration the physics of the problem studied. The use of homogeneous ones is not adequate in many cases (Geers et al., 2005). A POD decomposition of the flow is a good solution, because it takes into account the energetic distribution of the flow and gives information about the fluid energy distribution in the measurement domain for the acquisitions duration. The POD was introduced by Lumley (1967) for turbulent flows. Sirovich (1987) has introduced the snapshot POD which is useful when the spatial data size is much larger than the number of images, like PIV measurements. For this reason, the snapshot POD was used in this work.

Let us consider a sequence of PIV velocity fields $[\mathbf{U}(x, y, t_1), \ldots, \mathbf{U}(x, y, t_N)]$ taken at the discrete times $t_1, t_2, \ldots, t_N$. A POD decomposition of the flow consists in searching for a family of vectors $\left[\mathbf{\Phi}^{(1)}(x, y), \ldots, \mathbf{\Phi}^{(\mathrm{N})}(x, y)\right]$ on which $\boldsymbol{U}(x, y, t)$ can be decomposed as

$$\mathbf{U}(x, y, t_k) = \mathbf{U}_{\mathrm{mean}}(x, y) + \sum_{n=1}^{N} a^{(n)}(t_k)\mathbf{\Phi}^{(n)}(x, y) \tag{4}$$

with $\mathbf{U}_{\mathrm{mean}}$ is the mean time average velocity field, $k \in \{1, \ldots, N\}$ and $a^{(n)}(t)$ is the coefficient relative to $\mathbf{\Phi}^{(n)}(x, y)$.

The modes $\mathbf{\Phi}^{(n)}(x, y)$ verify, in this case, the following relation:

$$\langle \mathbf{\Phi}^{(n)}, \mathbf{\Phi}^{(m)} \rangle = \int_D \mathbf{\Phi}^{(n)}(x, y) \cdot \mathbf{\Phi}^{(m)}(x, y)\,\mathrm{d}x\,\mathrm{d}y = \delta_{n,m}, \tag{5}$$

where

$$\delta_{n,m} = \begin{cases} 1 & \text{if } n = m, \\ 0 & \text{if } n \neq m. \end{cases}$$

The temporal coefficients $a^{(n)}(t_j)$ verify the property

$$\sum_{j=1}^{N} [a^{(n)}(t_j)a^{(m)}(t_j)] = \lambda_n \delta_{n,m},$$

where λ_n is the eigenvalue associated to the spatial mode $\mathbf{\Phi}^{(n)}(x, y)$, and its weight in the flow.

To filter the PIV signal, Eq. (4) is truncated at the order M ($M<N$) as follows:

$$\mathbf{U}_{\text{filt}}(x,y,t_j)=\mathbf{U}_{\text{mean}}(x,y)+\sum_{n=1}^{M}a^{(n)}(t_j)\mathbf{\Phi}^{(n)}(x,y). \tag{6}$$

According to Sirovich (1987), the representative POD modes (or M-POD modes) must satisfy at least:

$$\left(\sum_{i=1}^{M}\lambda_i\Big/\sum_{i=1}^{N}\lambda_i\right)\geqslant 90\%.$$

For more details of the method see Appendix A.1.

4. Results and discussion

In order to determine the upstream flow conditions, 2-D PIV measurements were made in different sections and compared with the theoretical solution of Lundgren et al. (1964) (Fig. 3). The measurements are in good agreement with the theoretical results. According to Fig. 3(a), the boundary layer thickness upstream the cylinder in the span direction is about $5d_c$. The inflow may be considered uniform over $20d_c$ which permits to make comparison with the numerical 2-D simulations of Carte et al. (1995a, b) and Guerrouache (2000).

In the presence of a cylinder, PIV measurements permit extracting statistical information about the cylinder wake and decomposing the flow in three regimes like those found in the case of an unconfined cylinder (the steady 2-D, the unsteady 2-D and 3-D transition regime). They are discussed in the next sections with the modes calculated for measurement positions 1 and 2. Streamlines and path lines were calculated in the wake of the cylinder. The pathlines calculation was done using a 4th-order Runge-Kuta scheme, and the particle velocity is obtained using a bilinear interpolation. More details of this calculation scheme can be found in Harris et al. (1998).

For a fixed gap parameter and a confinement rate, the only parameter that controls the flow regime is the Reynolds number defined in our case as $\text{Re}=U_{\max}d_c/\nu$ where $U_{\max}=(3/2)U_m$ and $U_m=(1/3d_c)\int_{-1.5d_c}^{1.5d_c}U_{\text{mean}}(x,y)\,\mathrm{d}y$ is the height-averaged velocity given by PIV measurements, d_c is the cylinder diameter and ν is the kinematic viscosity of the fluid. It can be noticed here, that in the gap between the cylinder and the wall, the gap-averaged velocity is $U_m^{\text{gap}}=U_m/(2r)=U_{\max}/(3r)=U_{\max}$ because the confinement is $r=1/3$. Therefore, the Reynolds number previously defined is the same as the Reynolds number defined from the gap-averaged velocity.

4.1. Statistical results

Measurements taken at position 1 allows us to extract information about the wake flow in order to make comparison with a unconfined cylinder. In literature (Williamson, 1996; Paranthoën et al., 1999), the parameters most discussed are the dimensionless centreline velocity U_{cl}^*, the maximum of the fluctuations u_{rms}, v_{rms} of the velocity components at the centreline, the formation length L_F and the size of the mean recirculation region L_r.

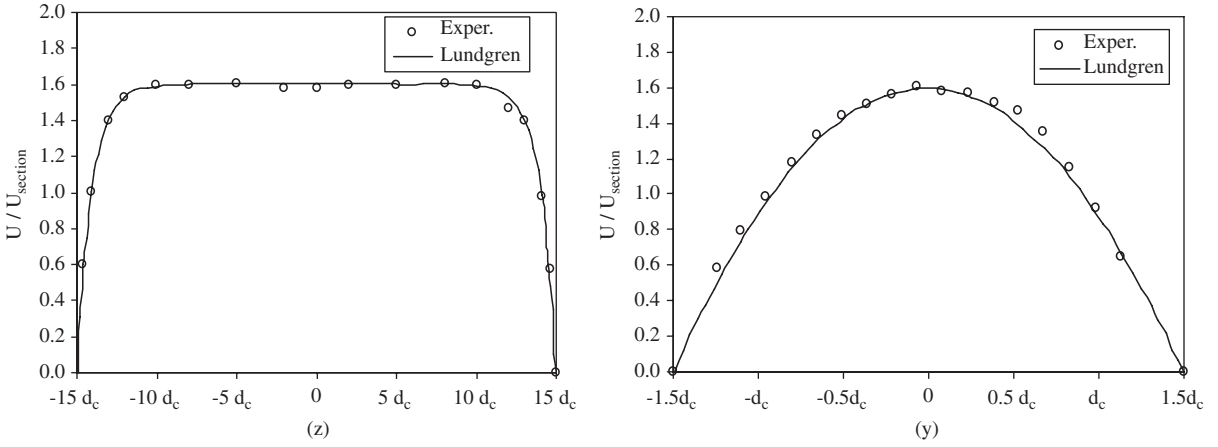

Fig. 3. Velocity profiles upstream of the cylinder: (a) section at $y=0$ and (b) section at $z=0$.

The dimensionless longitudinal centreline velocity downstream the cylinder is defined as $U^*_{cl} = U_{mean}(x,0)/U_m$. Fig. 4(a) gives the evolution of the centreline velocity with x-position for different Reynolds numbers. It also permits to calculate the mean recirculation region L_r for different Reynolds numbers (Fig. 4(b)), in order to make comparison with literature data obtained for unconfined cylinders. In Fig. 4(b), we distinguish two types of evolution. The first one, in the steady regime, is characterised by a linear evolution of L_r with Re, and the second one in the unsteady regime with L_r as a decreasing function of $Re^{-0.4}$. The maximum of $L_r = f(Re)$ is obtained for the critical Reynolds number Re_c, where the first instability appears (Paranthoën et al., 1999). In our case, we found $Re_c \approx 108$. This critical Reynolds number is in good agreement with the simulation results: Carte et al. (1995a, b) have found $Re_c \approx 97.5$, Guerrouache (2000) has given $Re_c \approx 100$ and Sahin and Owens (2004) obtained $Re_c \approx 101$. The size of the mean recirculation region in this confined case is greater than for the unconfined flows configuration (Fig. 4(b)). Its evolution with $(Re-Re_c)$ is less important than nunconfined cases. This is due to walls effect which are flattening and stabilising the mean recirculation region.

The quantities u_{rms}/U_m and v_{rms}/U_m, are symmetrical about the centreline. The position on the centreline, where u_{rms}/U_m is maximum, defines the formation length L_F (Williamson, 1996). Fig. 5(a) gives the evolution of the formation length L_F with the Reynolds number. It is a decreasing function with $Re-Re_c$ with exponent -0.3. It should be noticed that u_{rms}/U_m has two maxima shifted from the centreline, but the maximum of v_{rms}/U_m is on the centreline. The x-position of this maximum $\sigma^*_s = (v_{rms}/U_m)_{max}$ at the centreline is noted x_s. It was found experimentally that the value of σ^*_s is an increasing function of $Re-Re_c$ with an exponent of 0.4 (Fig. 5(b)), while it is about 0.34 in the case of a

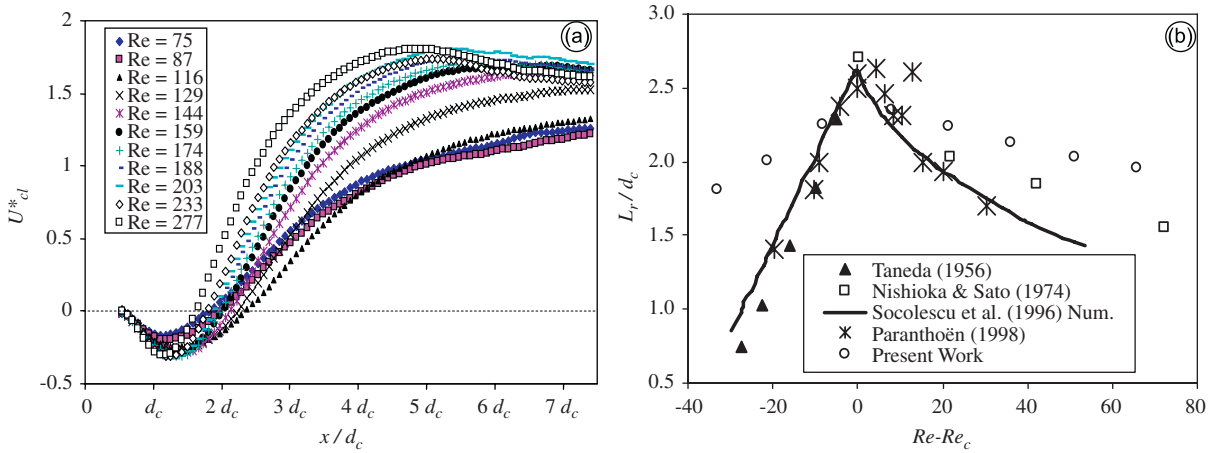

Fig. 4. (a) Streamwise evolution of the mean longitudinal velocity along the centreline in the cylinder wake and (b) evolution of mean recirculation region with $(Re-Re_c)$.

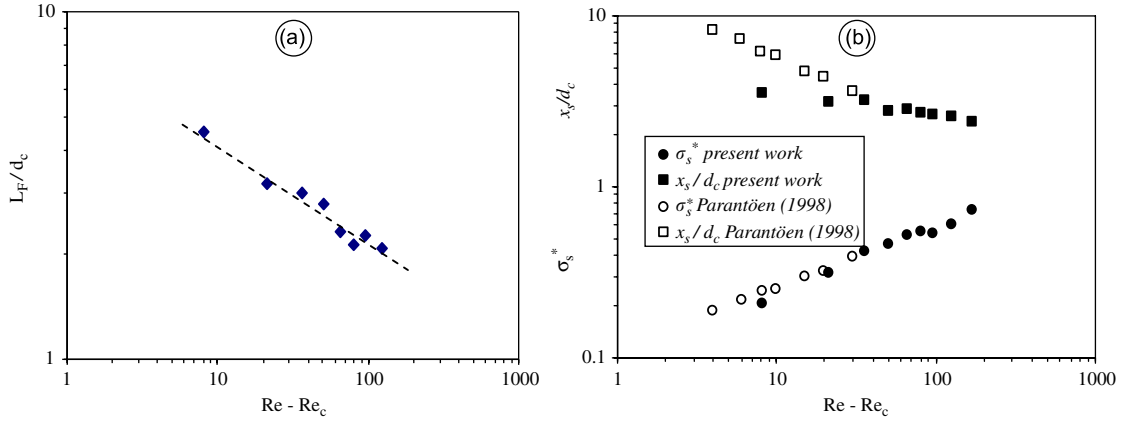

Fig. 5. (a) Evolution of the vortex length formation with $(Re-Re_c)$ and (b) evolution of x_s and σ^*_s with $(Re-Re_c)$: comparison with a unconfined cylinder case.

Table 1
Summary of the measured flow parameters

Re	$Re-Re_c$	U_m ($m\,s^{-1}$)	L_r/d_c	v_{rms} ($m\,s^{-1}$)	x_s/d_c	L_F/d_c	U_{ad} ($m\,s^{-1}$)	$Y_v/3d_c$	$(1/2)f_s$ (Hz)	k'' ($\times 10^5$) (m^{-1})	ω_{max} (s^{-1}) for $x = 10d_c$
75	−65	0.0050	1.817	–	–	–	–	–	–	–	–
87	−16	0.0058	2.009	–	–	–	–	–	–	–	–
100	−7	0.0067	2.247	–	–	–	–	–	–	–	0.92
116	8	0.0077	2.350	0.0016	3.552	4.515	–	–	0.30	–	–
129	21	0.0086	2.236	0.0027	3.154	3.217	0.01062	0.279	0.35	−0.83	–
144	36	0.0096	2.134	0.0040	3.176	3.013	0.01112	0.279	0.38	–	–
159	51	0.0106	2.032	0.0049	2.757	2.805	0.01276	0.304	0.43	−1.11	1.72
174	66	0.0116	1.964	0.0060	2.837	2.328	–	–	0.46	–	–
188	80	0.0126	1.907	0.0068	2.678	2.142	0.01448	0.297	0.50	−1.40	2.65
203	95	0.0135	1.884	0.0073	2.655	2.281	–	–	0.53	–	–
233	125	0.0155	1.805	0.0094	2.598	2.086	0.01689	0.297	0.61	−0.66	2.65
277	169	0.0185	1.658	0.0135	2.397	1.623	0.02081	0.297	0.72	−1.56	2.94

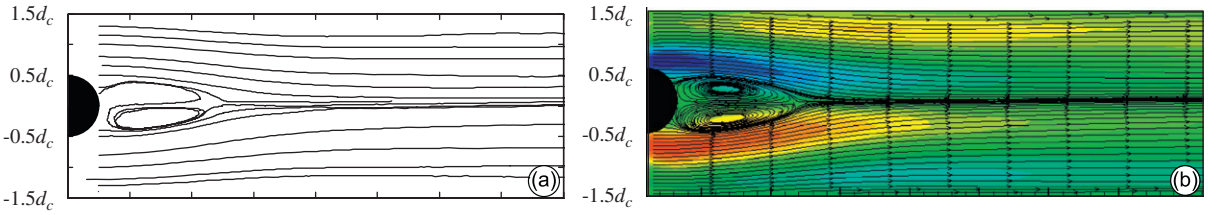

Fig. 6. Flow downstream of the cylinder for Re = 100: (a) Pathlines and (b) Vorticity and streamlines.

unconfined cylinder (Paranthoën et al., 1999). It can be noticed also that x_s is a decreasing function of $Re-Re_c$ with an exponent of −0.13 (Table 1), while the exponent is about −0.4 in the unconfined cylinder case (Paranthoën et al., 1999) (Fig. 5(b)), and x_s is more affected by the confinement than σ_s^*.

4.2. Steady regime

For $Re < Re_c \approx 108$, the flow is characterised by two fixed counter-rotating vortices downstream of the cylinder (Fig. 6(a) and (b)). The streamlines and the pathlines are confounded characteristics of a steady regime. The confinement delays the appearance of the von Kármán vortex shedding which should be about $Re \approx 47$ in an infinite medium. The walls give an irrotational effect due to the blocking by the body. The flow downstream of the cylinder (Fig. 6(b)) is constituted essentially of two fixed counter-rotating vortices located just behind the cylinder. The same topology is found in the case of a cylinder placed in an infinite medium. The only difference found in our case is the presence of a vorticity at walls which are opposite to the counter-rotating vortices.

4.3. Unsteady 2-D regime

When $Re \geqslant Re_c$, the wake becomes unstable with the appearance of the von Kármán vortices.

For Re = 129 (Fig. 7), the Γ_2 criterion allows to visualise a family of vortices (P_1, P_2) downstream the cylinder similar to those found in infinite medium. This family of vortices interacts with the two walls and generates a second family of vortices (P_1', P_2'). In fact, when the vortex P_1 (resp. P_2) is generated, the variation of vorticity near the lower (resp. upper) wall is accompanied by an interaction with the boundary layer manifested by the ejection of a vortex P_1' (resp. P_2') and a rejection of the vortex P_1, which has a positive circulation. This kind of interactions between the wall boundary layer and a vortex is detailed in the works of Escriva (1999). A von Kármán vortex P_2 (resp. P_1) detached from the upper (resp. lower) position of the cylinder does not remain in the upper (resp. lower) position like when the cylinder wake is in infinite medium, but it crosses the channel in the y-direction and rolls over the lower wall (resp. upper wall). These path intersections were observed by Guerrouache (2000) in their simulation. The generated vortex P_1' is advected in the

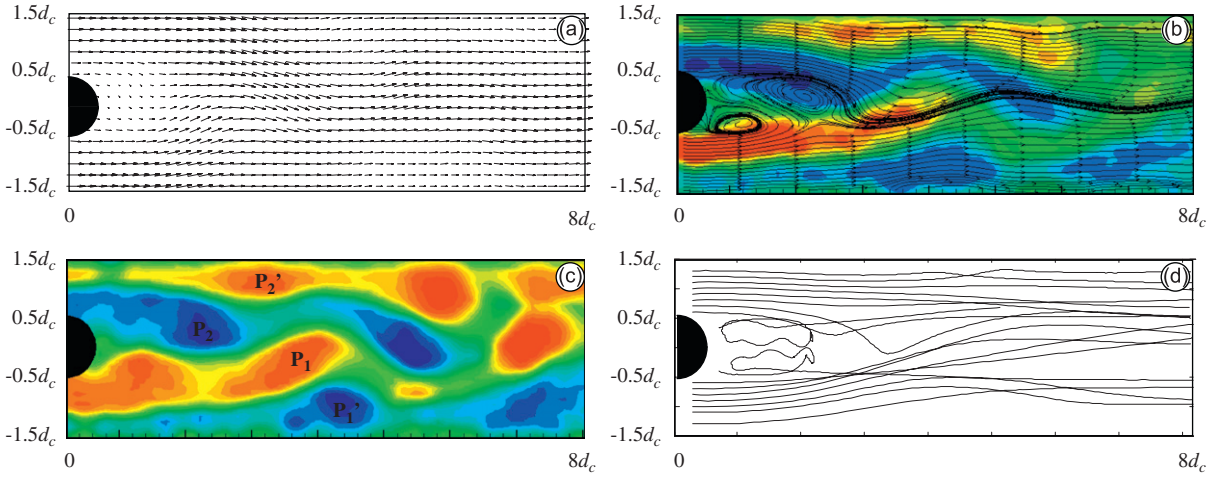

Fig. 7. Flow downstream of the cylinder for Re = 129: (a) velocity field; (b) vorticity and streamlines; (c) iso-Γ_2 criterion; and (d) pathlines.

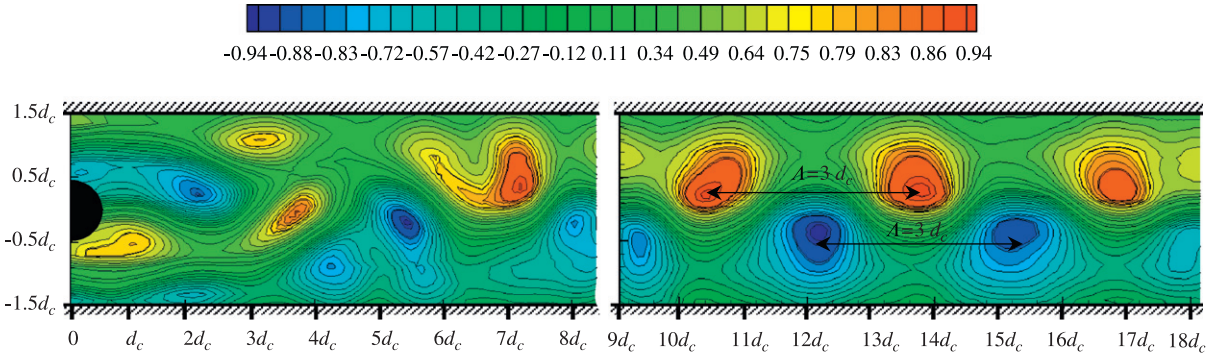

Fig. 8. Γ_2 criterion for Re = 159.

flow direction and coalesces with a vortex type P_2 at $x/d_c = 5$ to form a single vortex (Fig. 7(c)). The same remarks are also valid for the structures near the upper wall. For $x/d_c > 8$, the positive and negative vortices are spatially reorganised (Fig. 8). The distance between two similar vortices is $\Lambda = 3d_c$ with a transverse spacing between vortex centres about $1d_c$ and it was found to be independent of Reynolds in the range $\mathrm{Re}_c \leqslant \mathrm{Re} \leqslant 277$. In order to have information about the proper energy of the vortices in the cylinder wake, we have emphasise our analysis on the vortices placed for $x \geqslant 9d_c$. Two fundamental quantities are calculated: the advection velocity of a vortex and its contour. The vortex center at the time t_j is given by the methodology cited before. Fig. 9 gives the x-position versus time of a vortex center for different Reynolds numbers. It should be noticed that the y-position of the vortices was unchanged for $x \geqslant 9d_c$ in the range $\mathrm{Re}_c \leqslant \mathrm{Re} \leqslant 277$, and the advection velocity deduced from Fig. 9 is $U_{\mathrm{ad}} \approx (1.1 - 1.2)U_m$ (see Table 1). The vortices are in reality oval (Fig. 10(b) and (c)), and the calculation of the local velocity $\mathrm{U}_{\mathrm{loc}}(r, \theta, t) = \mathrm{U}(x, y, t) - \mathrm{U}_{\mathrm{ad}}$ (Fig. 10(b) and (d)) of the vortex shows that the radial component is not zero (Fig. 10(d)). In our case, we define the vortex limits by the positive values of the Q criterion around the vortex center. Its surface may be approximated (Fig. 10(a)) by a circle adjusted on the vortex center, and having a radius equal to the distance between the vortex center to the nearest wall y_v. The vortex can be seen as a rotating disk with a proper surface S_v. This may be a good approach and does not affect the calculations. Every point on the vortex surface is animated by a relative velocity defined in the vortex core as $\mathbf{U}_{\mathrm{loc}}(x, y, t) = \mathbf{U}(x, y, t) - \mathbf{U}_{\mathrm{ad}}$. The mean rotating energy of the vortex is thus defined by

$$E_C(t) = \frac{1}{S_v} \iint_{S_v} \frac{U_{\mathrm{loc}}^2(x, y, t)}{2} \, \mathrm{d}S. \tag{7}$$

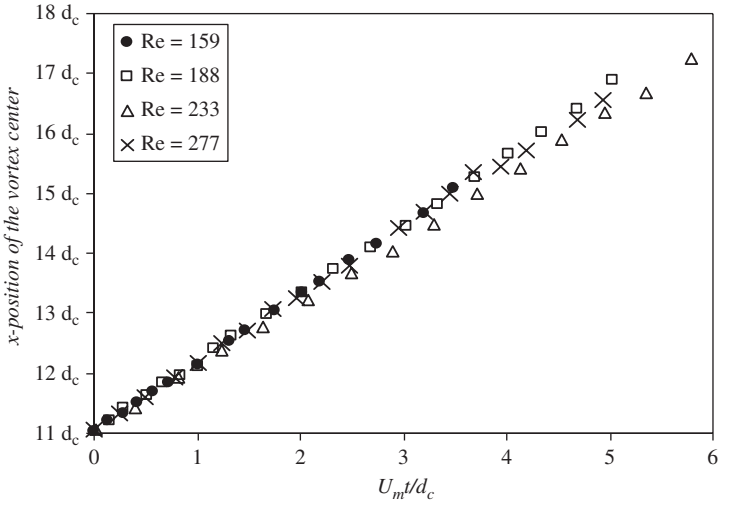

Fig. 9. Axial position of a vortex for different Reynolds numbers.

The dimensionless circulation of a vortex is defined as follows:

$$\Gamma^*(t) = \frac{\Gamma(t)}{2\pi\nu} = \frac{1}{2\pi\nu}\iint_{S_v} \omega(x,y,t)\,\mathrm{d}S, \tag{8}$$

where $\omega(x,y,t)$ is the vorticity, $\Gamma(t)$ is the circulation of the vortex and $\nu = 1.032\times10^{-6}\,\mathrm{m^2\,s^{-1}}$ is the kinematic viscosity of the fluid used at 25 °C.

The mean enstrophy of a vortex is defined in our case as

$$\mathrm{Enst}(t) = \frac{1}{S_v}\iint_{S_v} \frac{\omega^2(x,y,t)}{2}\,\mathrm{d}S. \tag{9}$$

Fig. 11(a) and (b) shows the degradation of $\Gamma^*(t)$ and the mean enstrophy during the vortex advection. At the highest Reynolds number considered (Re = 277), the decrease of enstrophy is the most important and it is essentially caused by the increase of the dissipation, the non-linearity and 3-D effects.

The mean enstrophy is another way to express the rotating energy of a vortex. In fact, in 2-D potential flows the conservation of enstrophy expresses the conservation of energy. So, it would be better to access to the rotating energy of a vortex from vorticity, but the presence of vortex deformation and 3-D effects influence this correlation between mean enstrophy and mean rotating energy of a vortex. In order to establish a relationship between $E_C(t)$ and $\mathrm{Enst}(t)$, we have plotted in Fig. 12(a) and for one vortex the quantity: $(8\pi/S_v)E_C(t) = f[\mathrm{Enst}(t)]$. It was found that

$$\left(\frac{8\pi}{S_v}\right)E_C(t) = C\,\mathrm{Enst}(t) + C_0, \tag{10}$$

where C is a dimensionless coefficient dependent on the Reynolds number (Fig. 12(b)) and $C_0 \in [0.1, 0.4]$ a bias. It should be noticed that for a solid rotating disk, we have $C = 1$ and $C_0 = 0$. This permits to conclude that the mean enstrophy is equivalent to the proper rotating energy of a vortex and for $\mathrm{Re} \leqslant 100$, the vortices can be seen as solid rotating disks and it is possible to neglect their deformation.

On the basis of the 2-D numerical studies of Carte et al. (1995a, b) and Guerrouache (2000) for $r = 1/3$ and $\gamma = 1$, the shedding frequency of vortices does not excced 2 Hz in the Reynolds numbers range studied. Hence, the experience is time resolved and permits the use of PIV to calculate the Strouhal number $\mathrm{St} = f_{\mathrm{st}} d_c / U_{\max}$. The PIV axial velocity at a fixed point in the domain is T-periodic. The frequency f_{St} is obtained from a spectrum of the PIV axial velocity at a fixed point in a domain containing vortices. Fig. 13 shows the evolution of $\mathrm{St}\cdot\mathrm{Re}$ with the Reynolds number in comparison to 2-D simulations of Carte et al. (1995a, b) and Guerrouache (2000) for the same confinenment rate of our experimental case. The evolution of $\mathrm{St}\cdot\mathrm{Re} = f(\mathrm{Re})$ can also be found with the Reynolds for unconfined cases given by Williamson (1992) which shows that the confinement shifts the evolution of $\mathrm{St}\cdot\mathrm{Re} = f(\mathrm{Re})$ upwards. Our experimental results are slightly higher than those obtained with these 2-D numerical simulations. In addition, by interpolating the

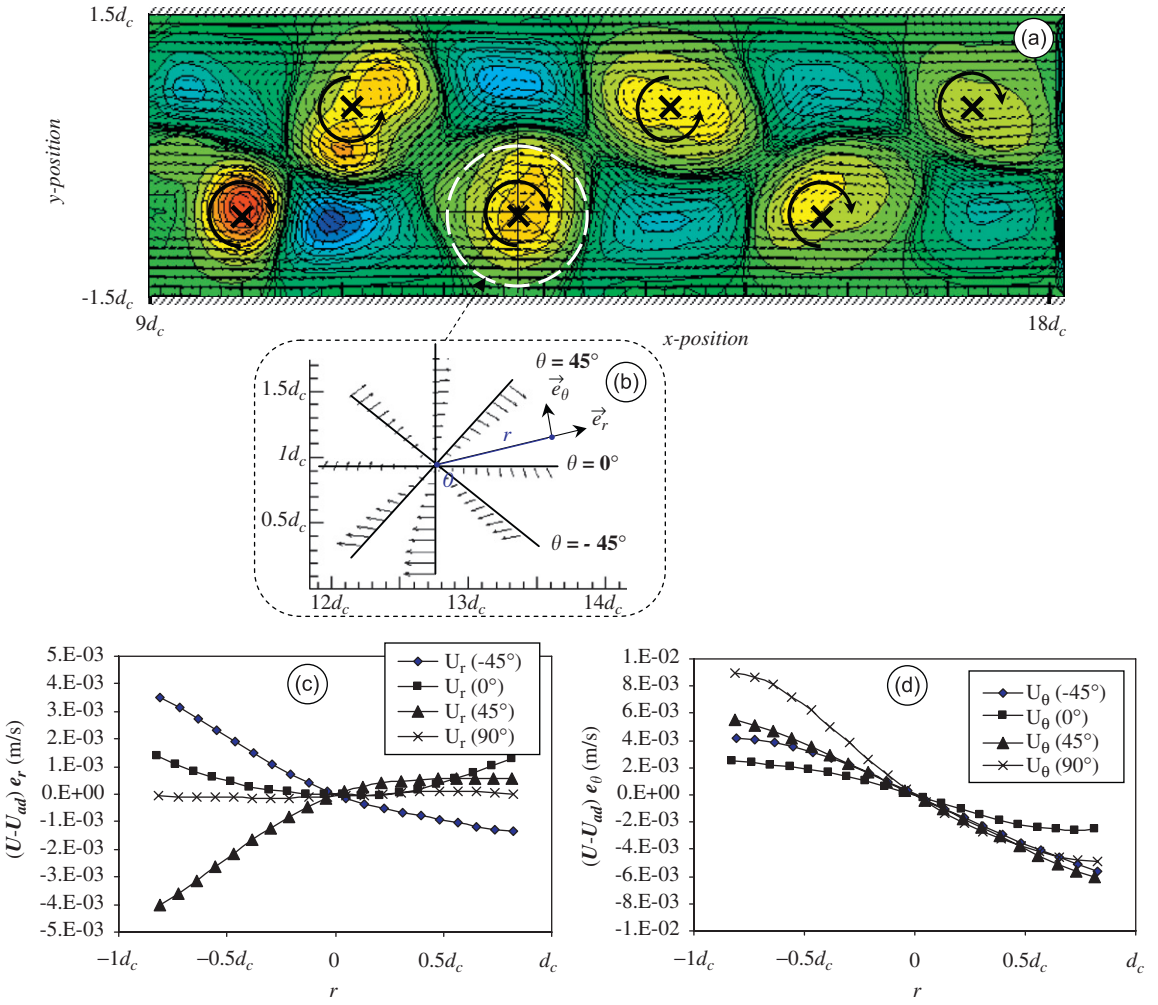

Fig. 10. (a) Field of ($\mathbf{U}-\mathbf{U}_{ad}$) superposed to Q criterion of the filtered velocity snapshot at Re = 159 (the vortices limits are marked with continious black curves); (b) typical relative velocity ($\mathbf{U}-\mathbf{U}_{ad}$) in the vortex core; (c) Radial local velocity in the vortex core; and (d) *ortho*-radial local velocity in the vortex core.

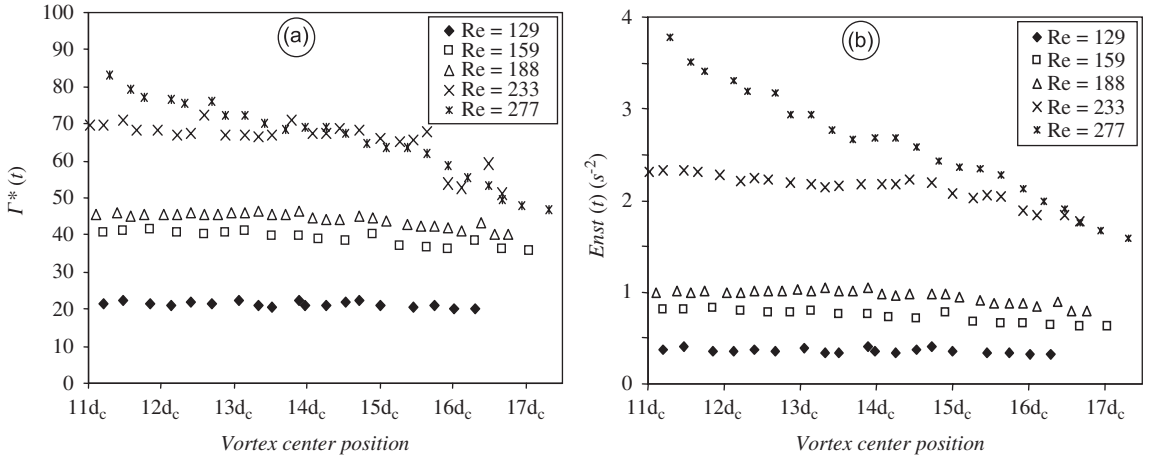

Fig. 11. Evolution for different Reynolds numbers of: (a) mean circulation and (b) mean enstrophy.

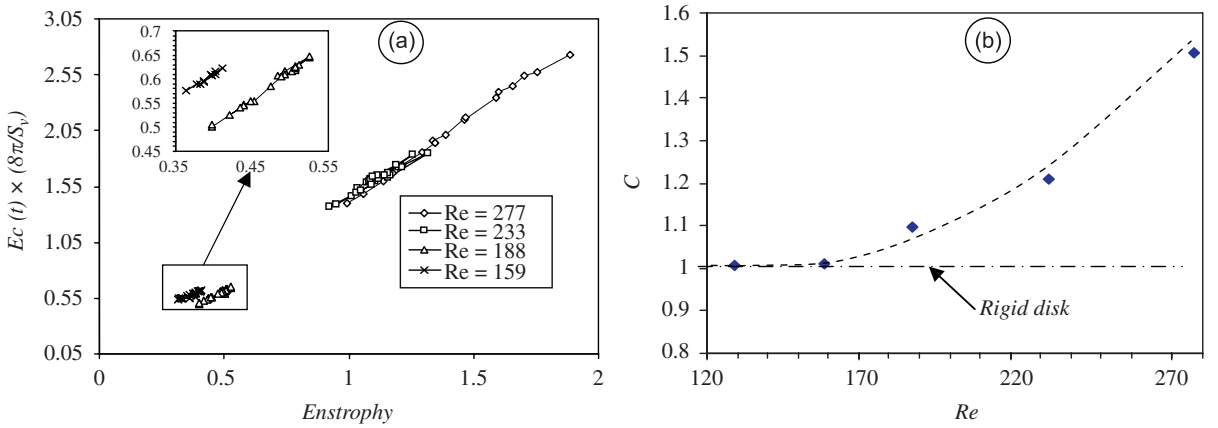

Fig. 12. (a) Evolution of the enstrophy with the local kinetic energy and (b) evolution of C with Re (Eq. (16)).

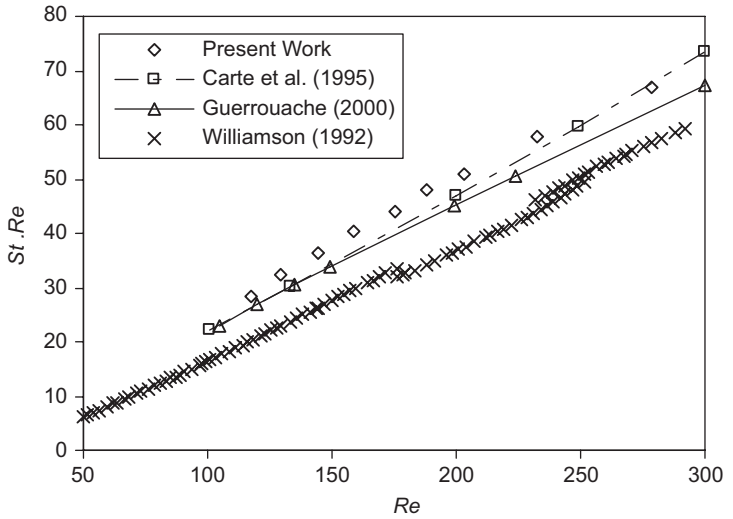

Fig. 13. Evolution of the Strouhal number with the Reynolds number.

recent stability analysis of Sahin and Owens (2004) for $r = 0.3$ and 0.5, it was found that $\mathrm{St} \approx 0.23$ for $\mathrm{Re} = \mathrm{Re}_c$, which is in good agreement with our experimental results. This result is in good agreement with the suggestions of Kang (2006) that the Strouhal number increases with increasing blockage.

It should be noted that if the Strouhal number is defined from the maximum of the velocity in the gap between the cylinder and the wall, i.e. its value is

$$\mathrm{St}^{\mathrm{gap}} = \frac{f_{\mathrm{St}} d_c}{U_m^{\mathrm{gap}}} = \frac{f_{\mathrm{St}} d_c}{U_{\max}/(1-r)}.$$

Therefore, the modified value will be $\mathrm{St}^{\mathrm{gap}} \approx 0.153$. These two values St and $\mathrm{St}^{\mathrm{gap}}$ are to be compared to the value 0.2 which corresponds to the shedding in infinite fluid at $\mathrm{Re} \approx 160$.

4.4. Three-dimensional effects

Three-dimensional instabilities can be detected using PIV measurements above the cylinder. The analysis of the flow above the cylinder in the range of Reynolds numbers $\mathrm{Re}_c \leqslant \mathrm{Re} \leqslant 188$, exhibits parallel rows shed behind the cylinder. The presence of undulations on the vortex core is the trace of a spanwise instability characterised by a wavelength

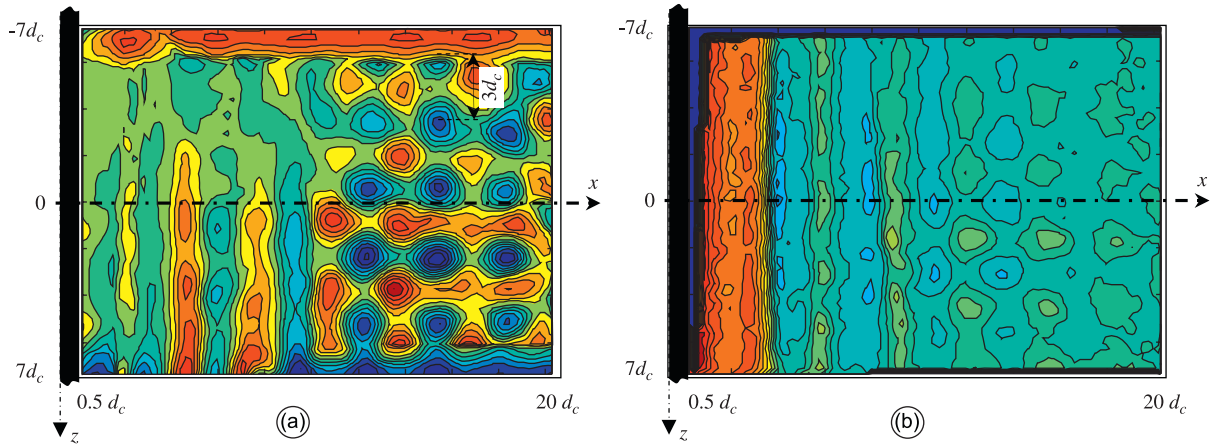

Fig. 14. Phase average of the velocity field at Re = 159: (a) iso-contours of Γ_2 criterion and (b) axial phase average velocity.

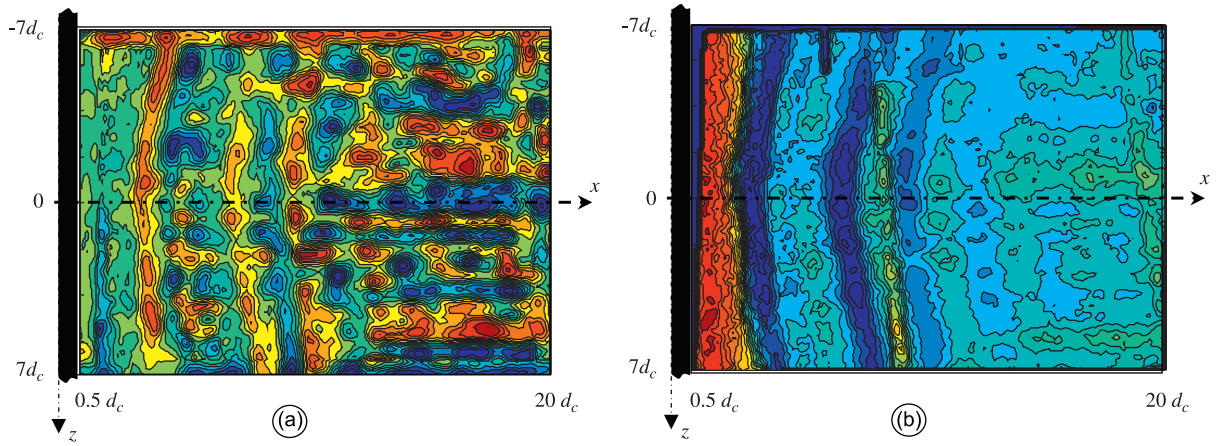

Fig. 15. Phase average of the velocity field for Re = 277: (a) iso-contours of Γ_2 criterion and (b) axial phase-averaged velocity.

$\Lambda_A \approx 3d_c$. Fig. 14 presents the phase-averaged velocity in the third position at Re = 159, and it exhibits the presence of spanwise instability. This instability is similar to that of "Mode A", which appears for the case of an unconfined cylinder at Re = 195 (Williamson, 1996). It seems that the premature appearance of "Mode A" at this range of Reynolds number is caused by the wall disturbance in the spanwise direction. By increasing the Reynolds number (Re $\geqslant$ 233), the von Kármán eddies adopt a non-parallel pattern and there is appearance of dislocations in the flow (Fig. 15). For the maximum Reynolds number studied (Re $\approx$ 277), the flow is similar to "Mode A*" found in the unconfined case. At Re $\approx$ 400, the measurements taken above the cylinder highlight the appearance of only longitudinal structures with a smaller scale ($\Lambda_B \approx d_c$) (Fig. 16). These structures are comparable to the "mode B" instabilities present in the case of a cylinder placed in a free stream for Re $\geqslant$ 260 (Williamson, 1996). It should be noticed that the instantaneous velocity field in position 3 exhibits the same topology with the phase-averaged one, but it was more interesting to present the phase-averaged velocity for the different Reynolds numbers.

5. POD decomposition and flow analysis

The POD decomposition of the flow was applied to the three experimental configurations cited before. It was verified that a number $N = 300$ of snapshots was sufficient for a statistical convergence of the data for a given Reynolds number. Table 2 shows a cumulative representation of the first six eigenvalues of the most energetic modes in both positions 1 and 2. It is worth noting that the POD decomposition was applied to the first and the second measurement

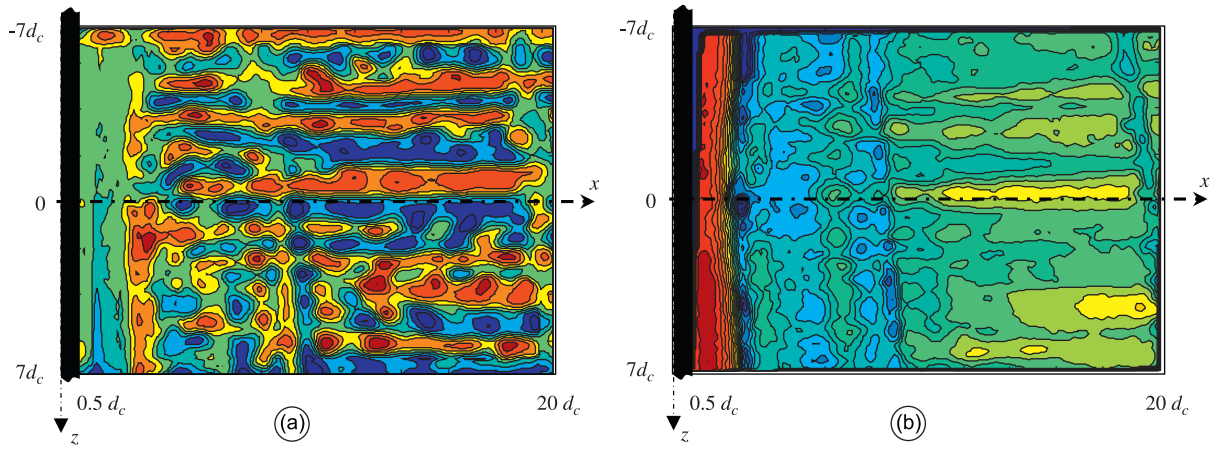

Fig. 16. Phase-average of the velocity field at Re = 400: (a) iso-contours of Γ_2 criterion and (b) axial phase-averaged velocity.

Table 2
Relative contribution, $\lambda_i/\sum_i\lambda_i$ of the first six eigenvalues for different Reynolds numbers

	Re = 129	Re = 144	Re = 159	Re = 188	Re = 233	Re = 277
Position 1						
Mode 1	0.453	0.446	0.455	0.456	0.462	0.450
Mode 2	0.431	0.437	0.444	0.445	0.446	0.417
Mode 3	0.021	0.028	0.027	0.026	0.021	0.023
Mode 4	0.021	0.027	0.026	0.026	0.015	0.022
Mode 5	0.012	0.009	0.008	0.009	0.015	0.009
Mode 6	0.009	0.008	0.008	0.009	0.005	0.009
Position 2						
Mode 1	0.411	0.455	0.484	0.476	0.482	0.432
Mode 2	0.390	0.427	0.464	0.456	0.446	0.391
Mode 3	0.039	0.029	0.012	0.014	0.021	0.027
Mode 4	0.036	0.027	0.011	0.013	0.013	0.020
Mode 5	0.026	0.010	0.005	0.009	0.012	0.014
Mode 6	0.013	0.009	0.003	0.004	0.006	0.013

positions separately. Hence, the issued spatial modes of each position should be interpreted independently and not as necessarily belonging to the same spatial modes of the entire flow.

The reconstruction of filtered data on the basis of these modes permits to recuperate more than 91% of the fluctuating flow energy since $(\sum_{i=1}^{6}\lambda_i/\sum_{i=1}^{N}\lambda_i)\geqslant 91\%$, which corresponds to more than 99% of the fluid energy when we consider the mean velocity field:

$$\left[\frac{(\langle \mathbf{U}_{\text{mean}}, \mathbf{U}_{\text{mean}}\rangle + \sum_{i=1}^{M}\lambda_i)}{\overline{\langle \mathbf{U}, \mathbf{U}\rangle}}\right] > 99\%.$$

The most energetic modes in position 1 of our measurements are the von Kármán harmonics. Their temporal coefficients $a^{(n)}(t)$ are sinusoidal, and may be written as follow (Fig. 17):

$$\begin{cases} a^{(n)}(t) = \sqrt{2\lambda_n}\cos\left[E\left(\dfrac{n+1}{2}\right)\Omega_s t + \xi_n\right], \\ a^{(n+1)}(t) = \sqrt{2\lambda_n}\sin\left[E\left(\dfrac{n+1}{2}\right)\Omega_s\Omega_s t + \xi_n\right], \end{cases} \tag{11}$$

where f_s is the shedding frequency, $\Omega_s = 2\pi f_s$ and $E((n+1)/2)$ is the integer part of $(n+1)/2$.

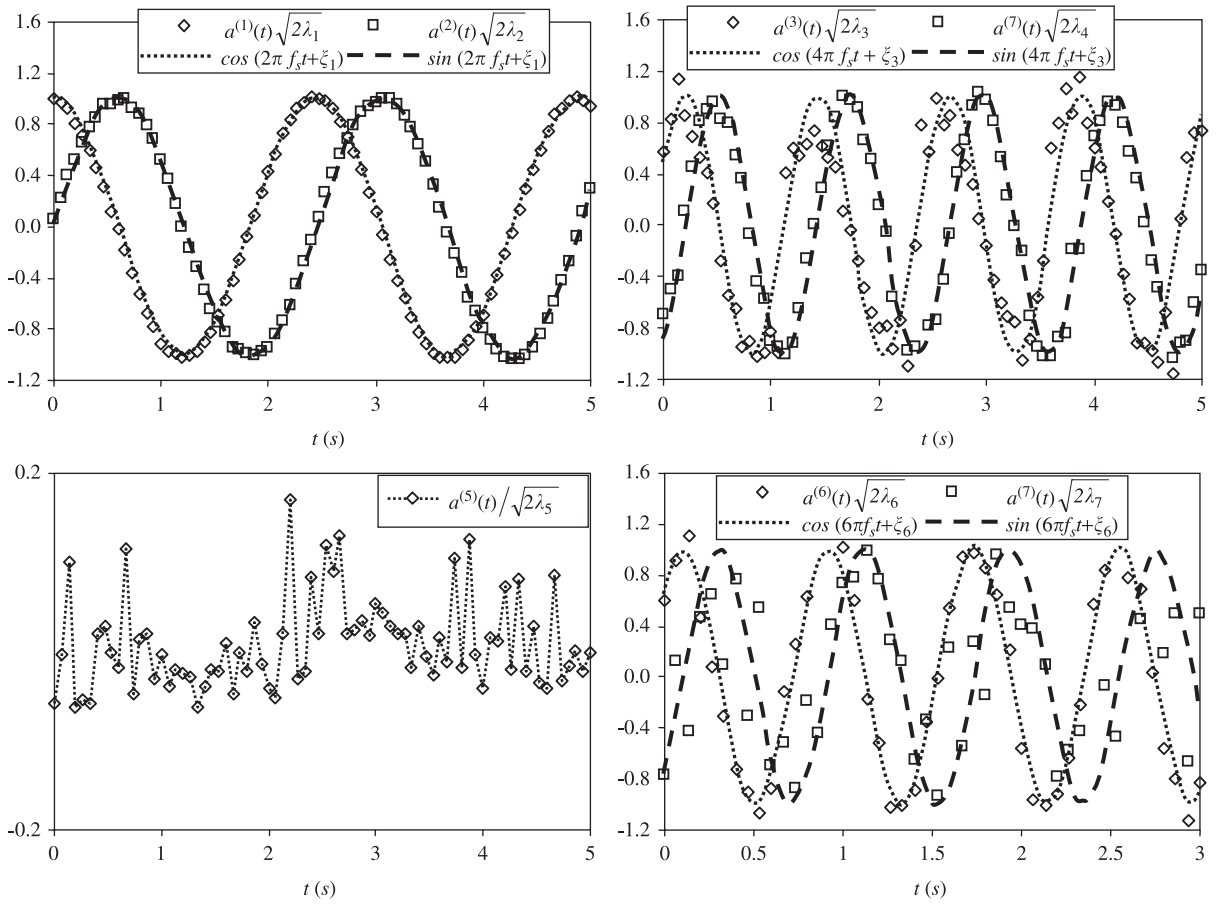

Fig. 17. Time evolution of the seventh first coefficients $a^{(n)}(t)$ for Re = 159, and for the second position.

It was found that these temporal modes are paired at Re = 100 for unconfined cylinder case (Ma et al., 2000). Ben Chiekh et al. (2004) and van Oudheusden et al. (2005) have found similar results for $a^{(1)}$ and $a^{(2)}$ in turbulent flows. The same remark can be made on the spatial coefficients $\mathbf{\Phi}^{(n)}$ which are also paired and which present a spatial pseudo-periodicity of $3d_c/E[(n+1)/2]$ (Figs. 18 and 19, left columns). For the measurement position 2 (Figs. 18 and 19, right columns), and in addition to the coherent modes found seen in position 1 of measurements with sinusoidal coefficients (Fig. 19, right column), the presence of incoherent modes was found. The energetic weight of these modes is more present in the second position, where the influence of the von Kármán vortex street is less intense. The incoherence of these modes can be seen in the temporal coefficients associated to these modes as $a^{(5)}$ (Fig. 17) at Re = 159 and its spatial mode $\mathbf{\Phi}^{(5)}$ in Fig. 18. The impact of these incoherent modes grows when increasing the Reynolds number like $\mathbf{\Phi}^{(3)}$ and $\mathbf{\Phi}^{(4)}$ at Re = 277 (Fig. 19) and could be caused by a deterioration of the steadiness in the flow at higher Reynolds numbers. Unfortunately, the analysis of the modes issued from the POD decomposition of the flow in position 1 and 2 did not give information about the transitions due to 3-D effects. Only the decomposition of the flow in position 3 informs about possible 3-D instabilities in the flow. Fig. 20 presents the first six energetic spatial POD modes of the flow from position 3 for Re = 159. The first and the second mode are conjugated, and they represent, respectively, the trace of the von Kármán eddies and their respective temporal coefficients $a^{(1)}$ and $a^{(2)}$. The latter are sinusoidal and periodic with a characteristic frequency of f_s. But one can see that these rollers, which are parallel, present traces of 3-D instabilities with a spatial periodicity in the spanwise direction of $\Lambda_A \approx 3d_c$. The Γ_2 criterion applied to the higher modes does not give interesting information, but it is to be noticed that $a^{(3)}$ and $a^{(4)}$ are periodic with a characteristic frequency of $2f_s$. When the Reynolds number increases, the three-dimensionality grows. At Re = 277, the first and the second spatial POD modes (Fig. 21) show that von Kármán roller traces are not parallel but with an arched shape, and the higher modes $\mathbf{\Phi}^{(3)}$, $\mathbf{\Phi}^{(4)}$, $\mathbf{\Phi}^{(5)}$ and $\mathbf{\Phi}^{(6)}$ present the trace of instabilities with longitudinal

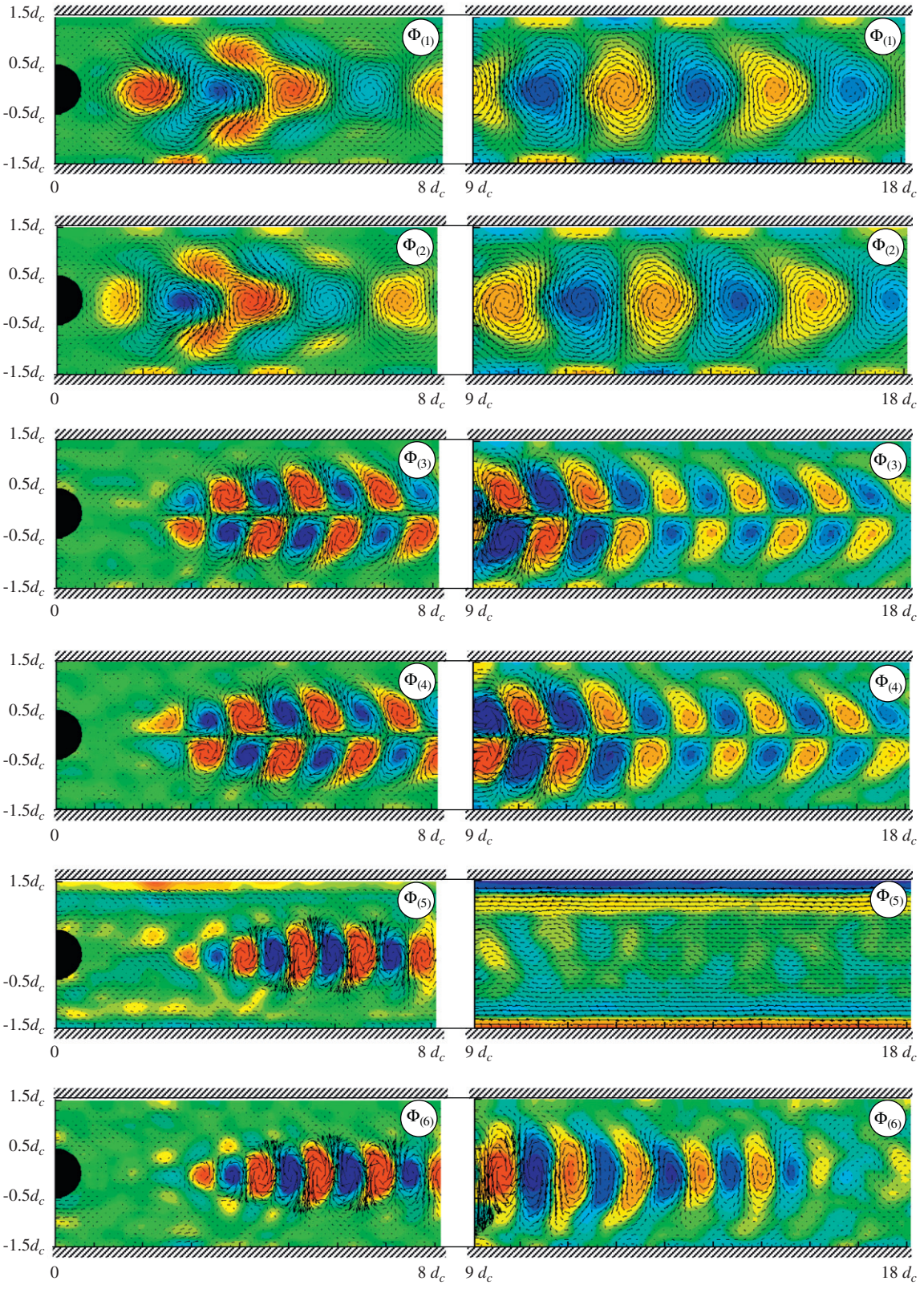

Fig. 18. The first six modes obtained downstream of the cylinder for Re = 159 (vector fields and vorticity maps): left column for position 1 of measurements and right column for the position 2 of measurements.

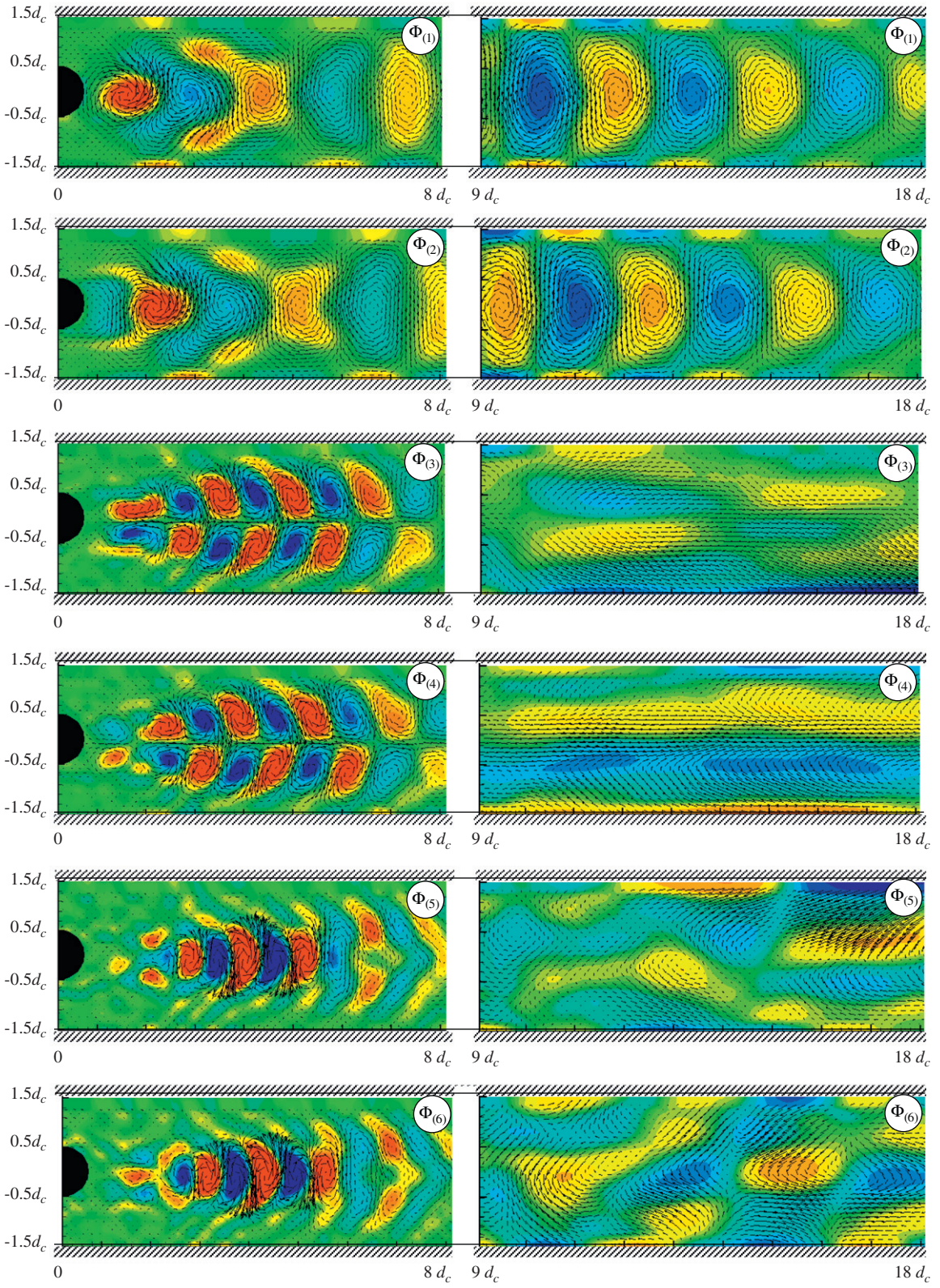

Fig. 19. The first six modes obtained downstream of the cylinder for Re = 277 (vector fields and vorticity maps): left column for position 1 of measurements and right column for the position 2 of measurements.

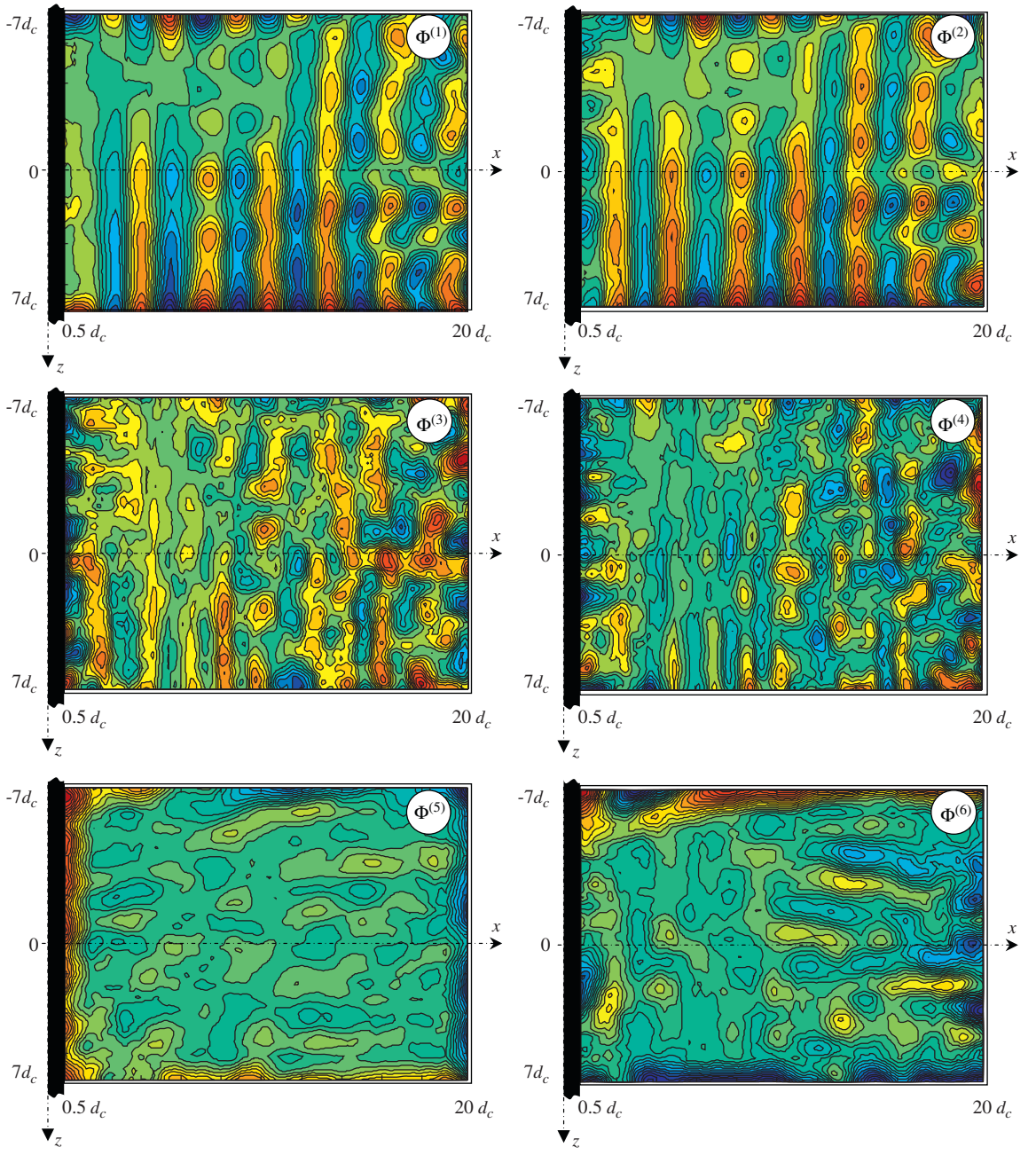

Fig. 20. Iso-contours of Γ_2 criterion applied to the first six most energetic modes for the third position measurements, and for Re = 159.

topology. This phenomenon becomes more and more obvious in the higher modes by increasing the Reynolds number. For example, at Re = 400, Fig. 22 exhibits longitudinal spanwise instabilities with a length scale of $\Lambda_B \approx 1d_c$. These longitudinal phenomena, which are more unstable, need a great number of modes $\mathbf{\Phi}^{(i)}$ to be correctly reconstructed by POD.

The mode pairing observed in this work and also reported by Ma et al. (2000) represents in reality the demonstration of vortex advection. In fact, the analysis of the POD paired modes in the second measurement position show that they

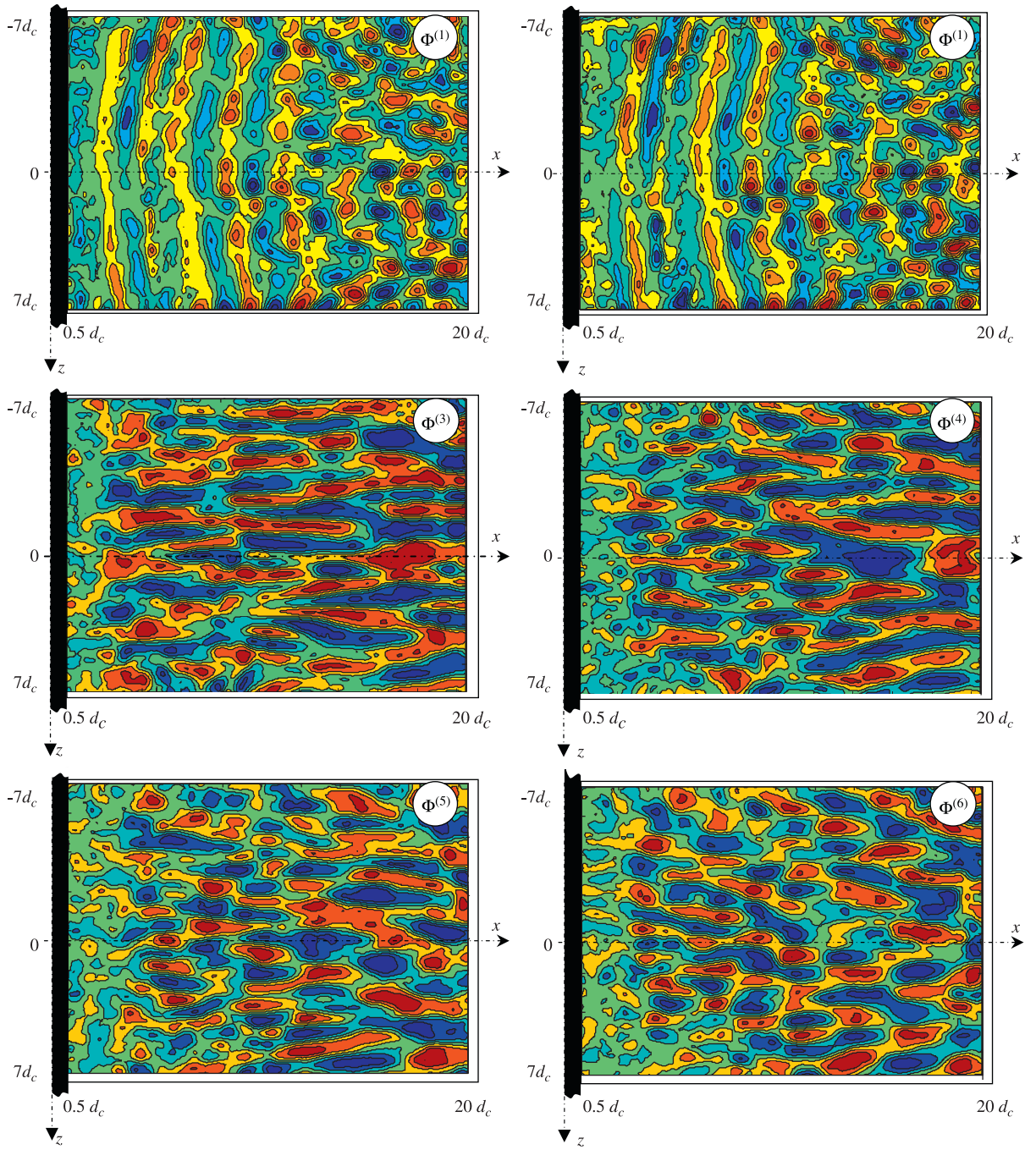

Fig. 21. Iso-contours of Γ_2 criterion applied to the first six most energetic modes for the third position measurements, and for Re = 277.

may be written as a sum of vanishing progressive waves (see Appendix A.2) as follows:

$$a^{(n)}(t)\mathbf{\Phi}^{(\mathbf{n})} + a^{(n+1)}(t)\mathbf{\Phi}^{(\mathbf{n+1})} = \mathrm{e}^{j\left(E\left(\frac{n+1}{2}\right)(\Omega_s t - \tilde{k}_s x)\right)}\mathbf{G}_n(y)$$

where $\tilde{k}_s = k'_s - \mathrm{j}k''_s$ is the wave complex number and where k''_s is a damping coefficient.

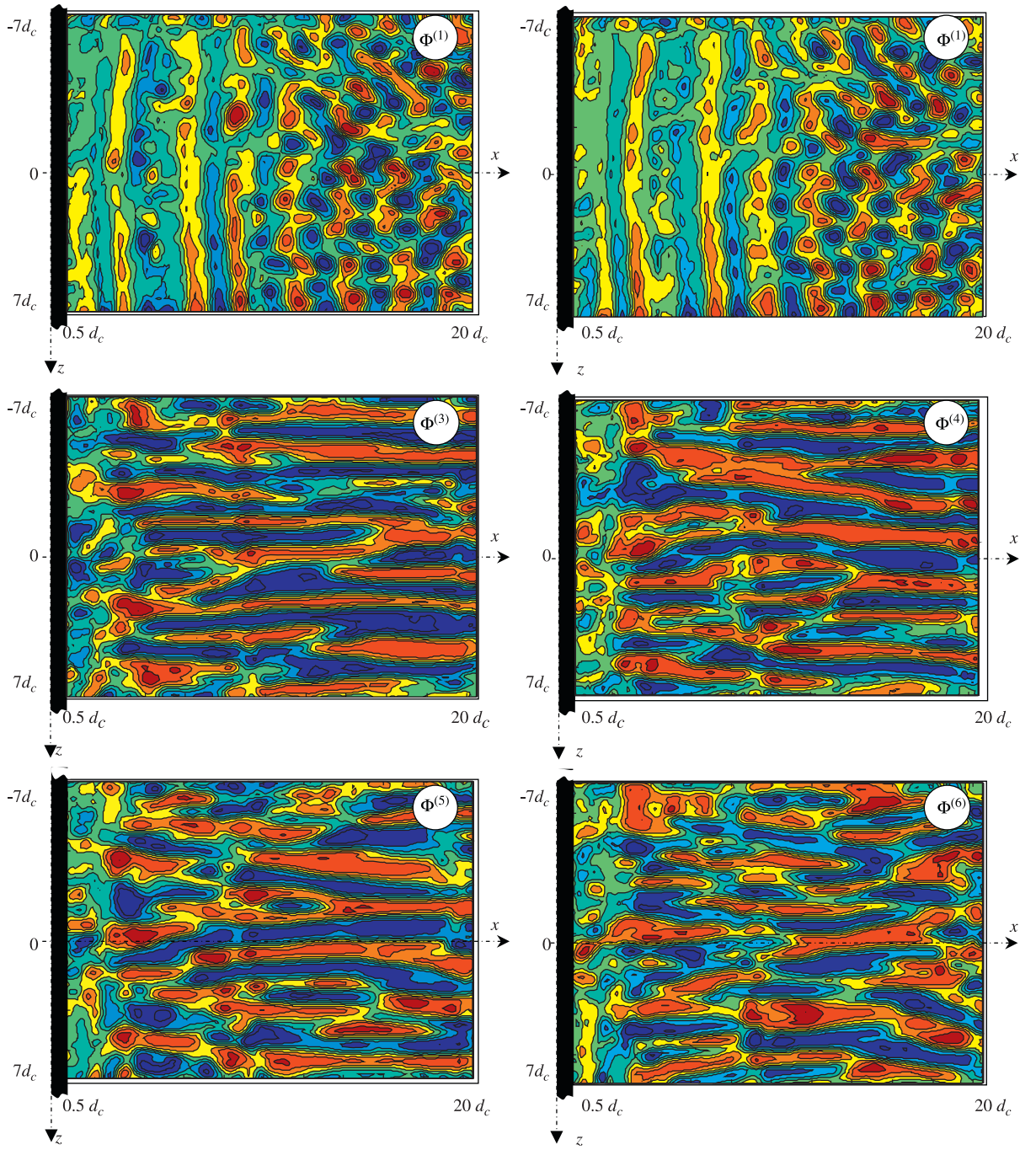

Fig. 22. Iso-contours of Γ_2 criterion applied to the first six most energetic modes for the third position measurements at Re = 400.

It is to be noticed also that the damping coefficient of the vortices k_s'' is an increasing function of the Reynolds number (i.e. of the shear). The exponential decrease of the energy of vortices as they are advected in the flow direction is due to viscous effects and to the imposed shear which is about $2/bU_{\max}$ at wall. The maximum vorticity values $\omega_{\max}$ obtained in the range of Reynolds number studied for $x = 13d_c$ (see Table 1) allow us to say that the erosion of the vortices is essentially due to the shear stress imposed (Paireau et al., 1997). Nevertheless, the vortices keep their integrity and their size for a large distance downstream the cylinder.

6. Conclusion

In this work, experimental investigation on the flow past a circular cylinder centred between parallel walls at low Reynolds numbers was studied using 2D–2C–PIV. The confinement was fixed at $r = 1/3$. Many differences were found in comparison with the unconfined cylinder case. The von Kármán instability which appears for the unconfined cylinder case at $\mathrm{Re} \approx 47$ is delayed to $\mathrm{Re}_c \approx 108$. It was also found that the wavelength of the von Kármán vortices is now about $\Lambda = 3d_c$ instead of $5d_c$ to $6d_c$ for the unconfined cylinder case. The analysis of the mean recirculation region and the rms of the velocity were also affected by the confinement and they show a stabilising effect induced by the walls. It was also noticed that the Strouhal number values are found to be in good agreement with the simulations of Sahin and Owens (2004). The comparison with the unconfined case PIV measurements in the span direction of the flow shows the presence of two types of 3-D instabilities similar to "Mode A" and "Mode B" for unconfined case in reference to Williamson (1996). The first instability present at $\mathrm{Re} \approx 159$ is similar to "Mode A" and characterised by a wavelength of $\Lambda_A \approx 3d_c$. By increasing the Reynolds number ($\mathrm{Re} \geqslant 277$), these instabilities become longitudinal and characterised by a wavelength of $\Lambda_b \approx 1d_c$. These longitudinal instabilities are similar to "Mode B" found in the unconfined case at $\mathrm{Re} \approx 230$–260. It seems that the "Mode A" instability appears earlier in the confined case which may be due to wall perturbations.

POD decomposition of the flow was used in this work in order to analyse the energetic contributions of the different modes, to extract the trace of the coherent structures present in the flow and to filter the different snapshots. The decomposition of the flow in the far wake shows equivalence with the Fourier decomposition, and the flow may be written as a sum of progressive damping waves (see Appendix A). We should also notice the presence of modes pairing reported also by Ma et al. (2000). In perspective, this decomposition will be used in a model reduction problem.

Appendix A

A.1. Snpashot POD decomposition background

Let $[\mathbf{U}(x,y,t_1),\ldots,\mathbf{U}(x,y,t_N)]$ be a sequence of PIV velocity fields taken at the discrete times $t_1, t_2, \ldots, t_N$. In order to calculate the different modes $\mathbf{\Phi}^{(n)}(x,y)$, we consider the temporal correlation matrix $\Re$ of the fluctuating velocities defined as

$$\Re = [\Re_{i,j}] = \frac{1}{N}\int_D [\mathbf{U}(x,y,t_i) - \mathbf{U}_{\mathrm{mean}}(x,y)] \cdot [\mathbf{U}(x,y,t_j) - \mathbf{U}_{\mathrm{mean}}(x,y)]\,\mathrm{d}x\,\mathrm{d}y. \tag{A.1}$$

The matrix $\Re$ is symmetric and positive. Let us note $\lambda_1 > \lambda_2 \cdots > \lambda_N > 0$ the N eigenvalues associated to $\Re$, and $\mathbf{V}^{(1)}$, $\mathbf{V}^{(2)}$, …, $\mathbf{V}^{(N)}$ their respective eigenvectors. The mode $\mathbf{\Phi}^{(n)}(x,y)$ is given by

$$\mathbf{\Phi}^{(n)}(x,y) = \sum_{j=1}^{N} \frac{V_j^{(n)}}{\sqrt{N\lambda_n}} \mathbf{U}(x,y,t_j). \tag{A.2}$$

Finally, the velocity field can be written as

$$\mathbf{U}(x,y,t_j) = \mathbf{U}_{\mathrm{mean}}(x,y) + \sum_{n=1}^{N} a^{(n)}(t_j)\mathbf{\Phi}^{(n)}(x,y), \tag{A.3}$$

where the coefficients $a^{(n)}(t_j)$ satisfy the property

$$\sum_{j=1}^{N} [a^{(n)}(t_j)a^{(m)}(t_j)] = \lambda_n \delta_{n,m}.$$

If $\overline{\langle \boldsymbol{f}, \boldsymbol{g} \rangle}$ is the time average of $\langle \boldsymbol{f}, \boldsymbol{g} \rangle$, and $\langle \boldsymbol{f}, \boldsymbol{g} \rangle = \int (f_x g_x + f_y g_y)\,\mathrm{d}x\,\mathrm{d}y$, we can write the eigenvalues of $\Re$ (which represent the energy weights of the different modes) as

$$\overline{\langle \mathbf{U}, \mathbf{U} \rangle} = \overline{\langle \mathbf{U}_{\mathrm{mean}}, \mathbf{U}_{\mathrm{mean}} \rangle} + \sum_{i=1}^{N} \lambda_i. \tag{A.4}$$

It must also be noted that, after a POD decomposition of the flow, the time evolution of the vorticity field for time-resolved measurements is obtained by the vorticity of the modes due to the linearity of the curl operator. We write

$$\boldsymbol{\omega}(x,y,t_j) = \frac{1}{2}\nabla \wedge \mathbf{U}(x,y,t_j) = \frac{1}{2}\nabla \wedge \mathbf{U}_{\mathrm{mean}}(x,y) + \frac{1}{2}\sum_{n=1}^{N} a^{(n)}(t_j)\nabla \wedge \mathbf{\Phi}^{(n)}(x,y). \tag{A.5}$$

In reality, the modes do not directly represent the flow structures but they are representative of the different spatial scales of the real coherent structures. The time-evolution of the coefficients $a^{(n)}$ is representative of the frequencies present in the flow. The filtered PIV signal, obtained from POD decomposition at the M order, allows us to write

$$\mathbf{U}_{\text{filt}}(x,y,t_j) = \mathbf{U}_{\text{mean}}(x,y) + \sum_{n=1}^{M} a^{(n)}(t_j)\boldsymbol{\Phi}^{(n)}(x,y), \tag{A.6}$$

$$\boldsymbol{\omega}(x,y,t_j) = \frac{1}{2}\nabla \wedge \mathbf{U}_{\text{mean}}(x,y) + \frac{1}{2}\sum_{n=1}^{M} a^{(n)}(t_j)\nabla \wedge \boldsymbol{\Phi}^{(n)}(x,y), \tag{A.7}$$

where

$$\left(\sum_{i=1}^{M}\lambda_i \Big/ \sum_{i=1}^{N}\lambda_i\right) \geqslant 90\%.$$

A.2. Temporal and spatial modes analysis in position 2 of measurements

In the case of wakes (Ben Chiekh et al. (2004), van Oudheusden et al. (2005)), and generally in flows presenting quasi-periodic moving vortices, the phenomenon of modes pairing is found. If $\boldsymbol{\Phi}^{(n)}$ and $\boldsymbol{\Phi}^{(n+1)}$ are two paired or conjugated modes, then their temporal coefficients will be given by the Eq. (17) and hence $a^{(n)}(t)\boldsymbol{\Phi}^{(n)} + a^{(n+1)}(t)\boldsymbol{\Phi}^{(n+1)}$ can be written as

$$a^{(n)}(t)\boldsymbol{\Phi}^{(n)} + a^{(n+1)}(t)\boldsymbol{\Phi}^{(n+1)} = \mathrm{e}^{\mathrm{j}\left(E\left(\frac{n+1}{2}\right)(\Omega_s t - k_s x)\right)}\mathbf{G}_n(x,y).$$

In the present study, especially, in the position 2 of measurements, the vortices are advected in the x-direction and the effect of the recirculating region is negligible. The purpose is to show that paired modes can be written as follows:

$$a^{(n)}(t)\boldsymbol{\Phi}^{(n)} + a^{(n+1)}(t)\boldsymbol{\Phi}^{(n+1)} = \mathrm{e}^{\mathrm{j}\left(E\left(\frac{n+1}{2}\right) \leftrightarrows (\Omega_s t - k_s x)\right)}\mathbf{G}_n(y). \tag{A.8}$$

For simplification purposes, we consider only the two first modes and the calculations will be identical in higher modes.

The two first functions $a^{(1)}(t)$ and $a^{(2)}(t)$ can be written as

$$a^{(1)}(t) = \sqrt{2\lambda_1}\,\cos(\Omega_s t + \xi_1), \quad a^{(2)}(t) = \sqrt{2\lambda_2}\,\sin(\Omega_s t + \xi_1), \tag{A.9}$$

where $\Omega_s = 2\pi f_{\text{st}}$.

Associating $\boldsymbol{\Phi}^{(1)}$ and $\boldsymbol{\Phi}^{(2)}$, we define for this first pair of modes the complex function:

$$\boldsymbol{\Psi}_1(x,y,t) = \mathrm{e}^{\mathrm{j}(\Omega_s t + \xi_1)}\left[\sqrt{2\lambda_1}\boldsymbol{\Phi}^{(1)}(x,y) - \mathrm{j}\sqrt{2\lambda_2}\boldsymbol{\Phi}^{(2)}(x,y)\right]. \tag{A.10}$$

According to Eq. (A.8), $\boldsymbol{\Psi}_1$ must be written as

$$\boldsymbol{\Psi}_1(x,y,t) = \mathrm{e}^{\mathrm{j}(\Omega_s\, t - \tilde{k}_s\, x)}\mathbf{G}_1(y), \tag{A.11}$$

where $\tilde{k}_s = k'_s - \mathrm{j}k''_s$ is the wave complex number. Then, the partial derivatives are linked by

$$\Omega_s \frac{\partial \boldsymbol{\Psi}_1}{\partial x} = -\tilde{k}_s \frac{\partial \boldsymbol{\Psi}_1}{\partial t}, \tag{A.12}$$

with $\boldsymbol{\Psi}_1$ given by Eq. (A.10), this relationship leads to:

$$k''_S\sqrt{\lambda_1}\boldsymbol{\Phi}^{(1)} + k'_s\sqrt{\lambda_2}\boldsymbol{\Phi}^{(2)} + \sqrt{\lambda_1}\frac{\partial \boldsymbol{\Phi}^{(1)}}{\partial x} = 0, \quad k'_S\sqrt{\lambda_1}\boldsymbol{\Phi}^{(1)} - k''_S\sqrt{\lambda_2}\boldsymbol{\Phi}^{(2)} - \sqrt{\lambda_2}\frac{\partial \boldsymbol{\Phi}^{(2)}}{\partial x} = 0. \tag{A.13}$$

The solution of this system, which is damped in the x-direction (with $k''_S > 0$), is

$$\boldsymbol{\Phi}^{(1)} = \mathbf{A}(y)\,\mathrm{e}^{-(k''_S - \mathrm{j}k'_S)x} + \mathbf{B}(y)\,\mathrm{e}^{-(k''_S + \mathrm{j}k'_S)x}, \quad \boldsymbol{\Phi}^{(2)} = \mathrm{j}\sqrt{\frac{\lambda_1}{\lambda_2}}(-\mathbf{A}(y)\,\mathrm{e}^{\mathrm{j}k'_S x} + \mathbf{B}(y)\,\mathrm{e}^{-\mathrm{j}k'_S x})\,\mathrm{e}^{-k'' x}, \tag{A.14}$$

where the components of $\mathbf{A}$ and $\mathbf{B}$ are complex.

If we choose the x-origin, so that the x-component of $\boldsymbol{\Phi}^{(1)}$ is

$$\Phi_x^{(1)} = b_x^{(1)}(y)\,\cos(k'_S x)\,\mathrm{e}^{-k''_S x}, \tag{A.15}$$

then

$$\Phi_x^{(2)} = b_x^{(1)}(y)\sqrt{\frac{\lambda_1}{\lambda_2}}\sin(k'_S x)\,\mathrm{e}^{-k''_S x}. \tag{A.16}$$

We may notice that the normalisation of $\mathbf{\Phi}^{(1)}$ and $\mathbf{\Phi}^{(2)}$ in (A.14) implies $\lambda_1 = \lambda_2$. This is confirmed by the experiment, which shows that the first two eignevalues agree within 5% at maximum (see Table 2).

Using the incompressible continuity equation $\nabla.\boldsymbol{\psi}_1 = 0$, we obtain for the y-components of $\mathbf{\Phi}^{(1)}$ and $\mathbf{\Phi}^{(2)}$:

$$\begin{cases} \dfrac{\partial \Phi_y^{(1)}}{\partial y} = b_x^{(1)}(y)[k'_S\,\sin(k'_S x) + k''_S\,\cos(k'_S x)]\,\mathrm{e}^{-k''_S x}, \\ \dfrac{\partial \Phi_y^{(2)}}{\partial y} = b_x^{(1)}(y)\sqrt{\dfrac{\lambda_1}{\lambda_2}}[k''_S\,\sin(k'_S x) - k'_S\,\cos(k'_S x)]\,\mathrm{e}^{-k''_S x}. \end{cases} \tag{A.17}$$

Experimentally, $k''_s/k'_s$is small (see Table 2). So,

$$\frac{\partial \Phi_y^{(1)}}{\partial y} = b_x^{(1)}(y)k'_S\,\sin(k'_S x)\,\mathrm{e}^{-k''_S x}, \quad \frac{\partial \Phi_y^{(2)}}{\partial y} = -b_x^{(1)}(y)\sqrt{\frac{\lambda_1}{\lambda_2}}k'_S\,\cos(k'_S x)\,\mathrm{e}^{-k''_S x}, \tag{A.18}$$

and for the first pair of modes, we have

$$a^{(1)}\Phi^{(1)} + a^{(2)}\Phi^{(2)} = b_x^{(1)}(y)\,\mathrm{e}^{-k''_s x}\,\cos(\Omega_s t - k'_s x) - k'_s\left(\int_0^y b_x^{(1)}(\eta)d\eta\right)\mathrm{e}^{-k''_s x}\,\sin(\Omega_s t - k'_s x). \tag{A.19}$$

The same results can be obtained for the second pair $\mathbf{\Phi}^{(3)}$ and $\mathbf{\Phi}^{(4)}$ at the frequency $2f_s$.

The examination of the experimental results for the far-wake measurements (position 2) conducts to factorising $\mathbf{\Phi}^{(1)}$ and $\mathbf{\Phi}^{(2)}$ by sinusoidal functions of period $3d_c$ in x:

$$\begin{aligned} \Phi^{(1)} &= \left[\cos\left(\frac{2\pi}{3d_c}x + \zeta_1\right)g_x^{(1)}\,\mathrm{sign}(y) - \sin\left(\frac{2\pi}{3d_c}x + \zeta_1\right)g_y^{(1)}\right], \\ \Phi^{(2)} &= \left[\sin\left(\frac{2\pi}{3d_c}x + \zeta_1\right)g_x^{(1)}\,\mathrm{sign}(y)\,\cos\left(\frac{2\pi}{3d_c}x + \zeta_1\right)g_y^{(1)}\right]. \end{aligned} \tag{A.20}$$

In fact, if $g_x^{(1)}(x,y)$ and $g_y^{(1)}(x,y)$ are defined by

$$g_x^{(1)}(x,y) = \sqrt{(\Phi_x^{(1)})^2 + (\Phi_x^{(2)})^2}, \quad g_y^{(1)}(x,y) = \sqrt{(\Phi_y^{(1)})^2 + (\Phi_y^{(2)})^2}$$

The values of the ratios $\Phi_x^{(1)}(x,y)/g_x^{(1)}(x,y)$ and $\Phi_y^{(1)}(x,y)/g_y^{(1)}(x,y)$, plotted in Fig. 23 for $y/d_c = 0.4$, 1.2, 1.8 and 2.8, are typical sinusoidal functions. That justifies the form of the system of Eq. (A.20).

The two values of λ_1 and λ_2 are very close. The eigenvalues related to the same pair of modes verify

$$\left|\frac{\lambda_i - \lambda_{i+1}}{\lambda_{i+1}}\right| \leqslant 3\%.$$

Using (A.19) and (A.20), we can write

$$a^{(1)}(t)\Phi^{(1)} + a^{(2)}(t)\Phi^{(2)} = \sqrt{2\lambda_1}\begin{bmatrix} g_x^{(1)}\cos\left(2\pi f_s t - \dfrac{2\pi}{3d_c}x + \chi_1\right)\mathrm{sign}\,(y) \\ g_y^{(1)}\sin\left(2\pi f_s t - \dfrac{2\pi}{3d_c}x + \chi_1\right) \end{bmatrix} \tag{A.21}$$

Now, by doing the same operations to the other conjugated modes, we can also write for the von Kármán harmonics of frequency $i \cdot f_s$:

$$a^{(i)}(t)\,\Phi^{(i)} + a^{(i+1)}(t)\Phi^{(i+1)} = \sqrt{2\lambda_i}\begin{bmatrix} \mathrm{sign}(y)\,g_x^{(i)}\,\cos\left(2\pi\,E\left(\dfrac{i+1}{2}\right)\left(f_s t - \dfrac{x}{3d_c}\right) + \chi_i\right) \\ g_y^{(i)}\,\sin\left(2\pi\,E\left(\dfrac{i+1}{2}\right)\left(f_s t - \dfrac{x}{3d_c}\right) + \chi_i\right) \end{bmatrix}. \tag{A.22}$$

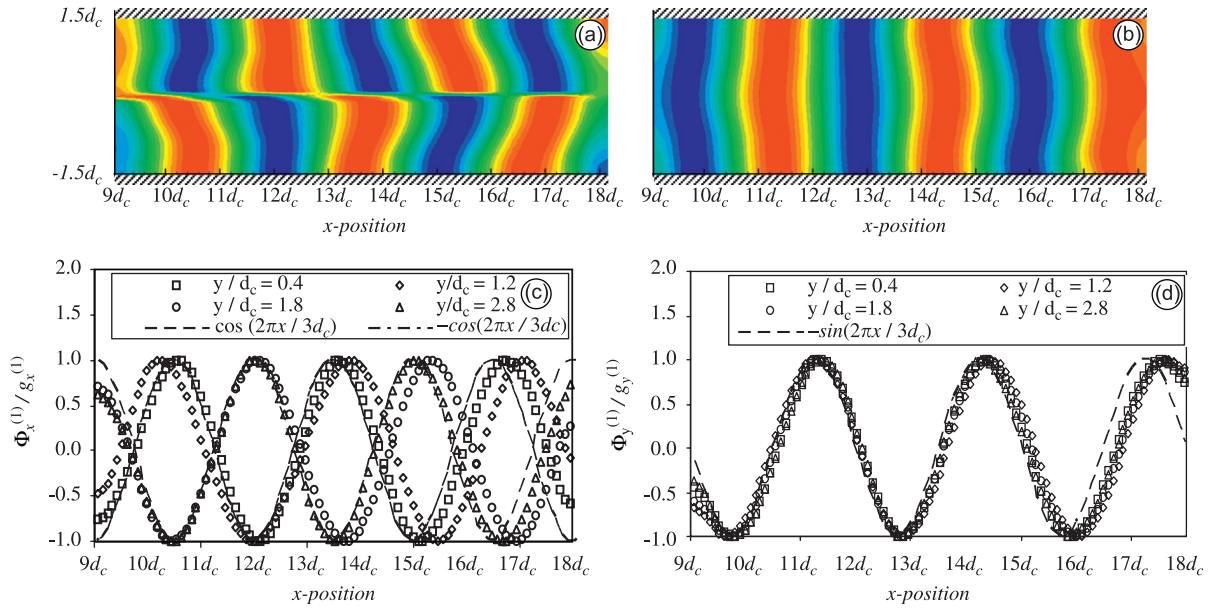

Fig. 23. Spatial evolutions of the functions: (a) $\Phi_x^1/g_x^{(1)}$, (b) $\Phi_y^1/g_y^{(1)}$, (c) $\Phi_x^1/g_x^{(1)}$ for different y/d_c values; and (d) $\Phi_x^1/g_y^{(1)}$ for different y/d_c values.

Finally, the velocity field can be written as follows:

$$\mathbf{U}_{\text{filt}}(x,y,t) = \mathbf{U}_{\text{mean}} + \sum_{i=1}^{E(M/2)} \sqrt{2\lambda_i} \begin{bmatrix} \text{sign}(y) g_x^{(i)} \cos\left(2\pi E\left(\frac{i+1}{2}\right)\left(f_s t - \frac{x}{3d_c}\right) + \chi_i\right) \\ g_y^{(i)} \sin\left(2\pi E\left(\frac{i+1}{2}\right)\left(f_s t - \frac{x}{3d_c}\right) + \chi_i\right) \end{bmatrix} + \sum_{\text{incoherent}} a^{(i)}\boldsymbol{\Phi}^{(i)}, \quad \text{(A.23)}$$

where $\sum_{\text{incoherent}} a^{(k)}\boldsymbol{\Phi}^{(k)}$ is the non coherent part (not related to the von Kármán vortices) of the POD decomposition.

Eq. (A.23) permits to see the travelling vortices as a sum of progressive damped waves ($g_x^{(k)}$ and $g_y^{(k)}$ are decreasing functions of x). In order to verify the assumptions given by the Eq. (A.11), we restrict for simplification the calculations to the first pair of POD modes and we have to compare the predicted form given by Eq. (A.19) with Eq. (A.21).

By identification, we obtain

$$\sqrt{2\lambda_1} g_x^{(1)}(x,y)\,\text{sign}(y) = b_x^{(1)}(y)\,\mathrm{e}^{-k_s'' x},\ \sqrt{2\lambda_1} g_y^{(1)}(x,y) = k_s' \left[\int_0^y \text{sign}(\eta) b_x^{(1)}(\eta)\,\mathrm{d}\eta\right] \mathrm{e}^{-k_s'' x}. \quad \text{(A.24)}$$

To verify the validity of the Eq. (A.24) for $x/d_c \geqslant 13$, we can proceed in two steps. The first step consists in verifying that the functions $g_x^{(1)}(x,y)$ and $g_y^{(1)}(x,y)$ can be written as

$$g_x^{(1)}(x,y) = p_x^{(1)}(x) q_x^{(1)}(y), \quad g_y^{(1)}(x,y) = p_x^{(1)}(x) q_y^{(1)}(y). \quad \text{(A.25)}$$

The second step consists in verifying that

$$p_x^{(1)}(x) = \alpha\,\mathrm{e}^{k_s'' x}, \quad q_y^{(1)}(y) = \beta \int_0^y \text{sign}(\eta) q_x^{(1)}(\eta)\,\mathrm{d}\eta, \quad \text{(A.26a,A.26b)}$$

where α and β are two constants.

The values of $p_x^{(1)}$ are estimated by averaging $g_x^{(1)}$ on the height of the channel. So, the function $p_x^{(1)}(x)$ is defined as

$$p_x^{(1)}(x) = \frac{1}{3d_c} \int_{-1.5d_c}^{1.5d_c} g_x^{(1)}(x,y)\,\mathrm{d}y, \quad \text{(A.27)}$$

noticing that the α value in Eq. (A.26a) may be arbitrarily chosen.

Fig. 24 gives the evolution of $p_x^{(1)}$ along the x-position for different Reynolds numbers. It is to be noted that for $x \geqslant 13d_c$, function $p_x^{(1)}$ can be expressed as a decreasing exponential function with a slope k'' (see Table 1).

We define the functions $q_x^{(1)}(x,y)$ and $q_y^{(1)}(x,y)$ by the following expressions:

$$q_x^{(1)}(x,y) = \frac{g_x^{(1)}}{p_x^{(1)}}, \quad q_y^{(1)}(x,y) = \frac{g_y^{(1)}}{p_x^{(1)}}. \tag{A.28}$$

Fig. 25(a)–(d) shows that $q_i^{(1)}(x,y) \approx q_i^{(1)}(y)$ (for $i \in \{x,y\}$) and the separation of variables Eq. (A.25) is well justified.

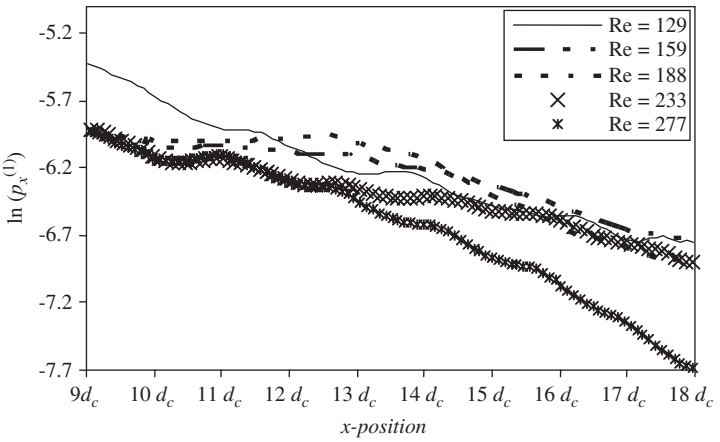

Fig. 24. Spatial evolution of $p_x^{(1)}$ for different Reynolds numbers.

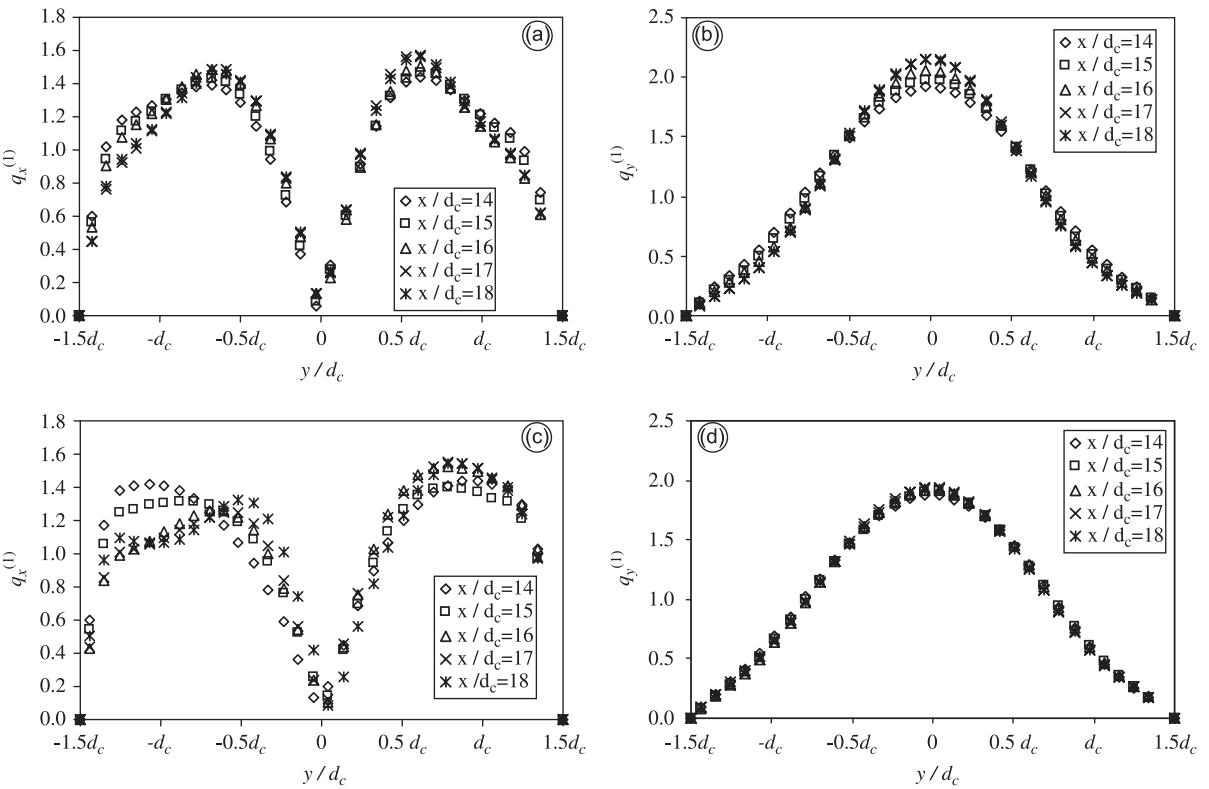

Fig. 25. $q_x^{(1)}$ and $q_y^{(1)}$ versus y for different values of x/d_c: (a) $q_x^{(1)}$ for Re = 159; (b) $q_y^{(1)}$ for Re = 159; (c) $q_x^{(1)}$ for Re = 277; and (d) $q_y^{(1)}$ for Re = 277.

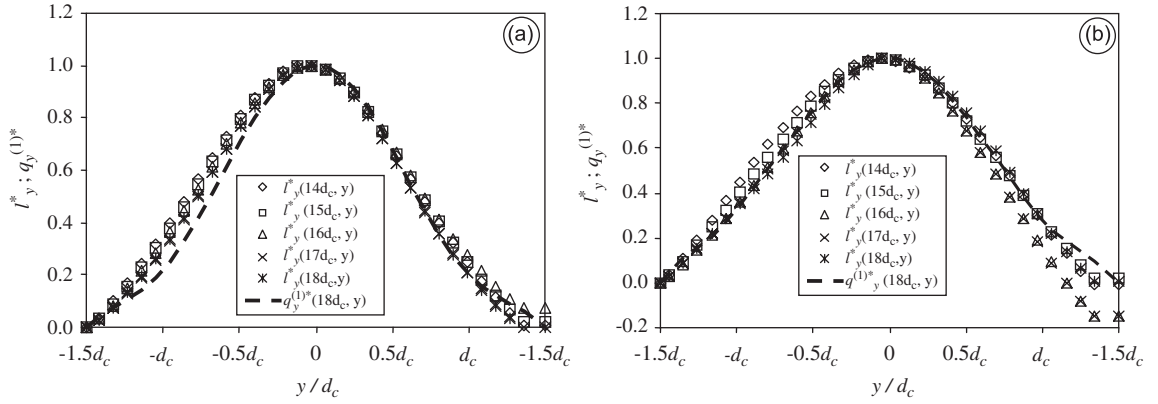

Fig. 26. l^*_y and $q^{(1)^*}_y$ versus y for different values of x/d_c: (a) Re = 159 and (b) Re = 277.

Fig. 26(a) and (b) gives a comparison between the normalised functions

$$q^{(1)^*}_y = q^{(1)}_y / q^{(1)}_y(0) \tag{A.29}$$

and the quantity

$$l^*(y) = \int_0^y \text{sign}(\eta) q^{(1)}_x(\eta)\, d\eta \Big/ \left[\int_0^{1.5d_c} \text{sign}(\eta) q^{(1)}_x(\eta)\, d\eta\right].$$

The concordance between the two results permits to confirm that $q^{(1)}_y$ may be deduced from $q^{(1)}_x$ by integrating Eq. (A.26a).

This result proves that, in our case, the paired modes in the position 2 of measurements satisfy Eqs. (A.8) and (A.11), which permits also to see the flow as a sum of propagating vanishing waves.

References

Anagnostopoulos, P., Iliadis, G., Richardson, S., 1996. Numerical study of the blockage effect on viscous flow past a circular cylinder. International Journal for Numerical Methods in Fluids 22, 1061–1074.

Bearman, P.W., Zdravkovich, M.M., 1978. Flow around a circular cylinder near a plane boundary. Journal of Fluid Mechanics 89, 33–47.

Ben Chiekh, M., Michard, M., Grosjean, N., Bera, J.C., 2004. Reconstruction temporelle d'un champ aérodynamique instationnaire à partir de mesures PIV non résolues dans le temps. In: Proceedings of 9ème congrès Francophone de Vélocimétrie Laser, D.8, 14–17 September, Brussels, Belgium.

Braza, M., Perrin, R., Hoarau, Y., 2006. Turbulence properties in the cylinder wake at high Reynolds numbers. Journal of Fluids and Structures 22, 757–771.

Brede, M., Eckelmann, H., Rockwell, D., 1996. On secondary vortices in the cylinder wake. Physics of Fluids 8, 2117–2124.

Carte, G., Dusek, J., Fraunié, P., 1995a. A spectral time discretization for flows with dominant periodicity. Journal of Computational Physics 120, 171–183.

Carte, G., Dusek, J., Fraunié, P., 1995b. A combined spectral-finite difference time discretization for periodic and quasi-periodic flows. Journal of Computational and Applied Mathematics 63, 245–254.

Chen, J.H., Pritchard, W.G., Tavener, S.J., 1995. Bifurcation for flow past a cylinder between parallel planes. Journal of Fluid Mechanics 284 (5), 23–41.

Coutanceau, M., Defaye, J.R., 1991. Circular cylinder wake configurations: a flow visualization survey. Applied Mechanics Reviews 44, 255–305.

Coutanceau, M., Bouard, R., 1977. Experimental determination of the main features of the viscous flow in the wake of a cylinder in uniform translation. Part 1: Steady flow. Journal of Fluid Mechanics 79, 231–256.

Escriva, X., 1999. Étude dynamique et thermique des transferts pariétaux instationnaires: Application à l'interaction tourbillon couche limite. Ph.D. Thesis, Université Paul Sabatier, France.

Geers, L.F.G., Tummers, M.J., Hanjalic, K., 2005. Particle imaging velocimetry-based identification of coherent structures in normally impinging multiple jets. Physics of Fluids 17, 1–13.

Graftieaux, L., Michard, M., Grosjean, N., 2001. Combining PIV, POD and vortex identification algorithms for the study of unsteady turbulent swirling flows. Measurements and Science Technology, 1422–1429.

Guerrouache, M.S., 2000. Étude numérique de l'instabilité de Bénard-Kármán derrière un cylindre fixe ou en mouvement périodique. Dynamique de l'écoulement et advection chaotique. Ph.D. Thesis, Université de Nantes.

Haller, G., 2005. An objective definition of a vortex. Journal of Fluid Mechanics 525, 1–26.

Harris, J., Harris, W., Stocker, H., 1998. Handbook of Mathematics and Computational Science. Springer, New York.

Hunt, J.C., Wray, A.A., Moin, P., 1988. Eddies, Stream and Convergence Zones in Turbulent Flows. Center for Turbulence Research Report, Stanford, CTR-S88, pp. 193–208.

Kang, S., 2006. Uniform-shear flow over a circular cylinder at low Reynolds numbers. Journal of Fluids and Structures 22, 541–555.

Karniadakis, G.E.M., Triantafyllou, G.S., 1989. Frequency selection and asymptotic states in laminar wakes. Journal of Fluid Mechanics 199, 441–469.

Lei, C., Cheng, L., Kavanagh, K., 1999. Re-examination of the effects of a plane boundary on force and vortex shedding of a circular cylinder. Journal of Wind Engineering and Industrial Aerodynamics 80, 263–286.

Lumley, J.L., 1967. The structure of inhomogeneous turbulence. In: Atmospheric Turbulence and Radio Wave Propagation, Yagolm AL, Tatarskiva Editions, Nauka, Moscow, pp. 166–178.

Lundgren, T.S., Sparrow, E.M., Starr, J.B., 1964. Pressure drop due to the entrance region in ducts of arbitrary cross section. ASME Journal of Basic Engineering 86, 620–626.

Ma, X., Karamanos, G.-S., Karniadakis, G.E., 2000. Dynamics and Low-Dimensionality of a Turbulent Near Wake 410, 29–65.

Paireau, O., Tabeling, P., Legras, B., 1997. A vortex subjected to a shear: an experimental study. Journal of Fluid Mechanics 351, 1–16.

Paranthoën, P., Browne, L.W.B., Le Masson, S., Dumouchel, F., Lecordier, J.C., 1999. Characteristics of the near wake of a cylinder at low Reynolds numbers. European Journal of Mechanics B/Fluids 18, 659–674.

Price, S.J., Sumner, D., Smith, J.G., Leong, K., Païdoussis, M.P., 2002. Flow visualization around a circular cylinder near to a plane wall. Journal of Fluids and Structures 16, 175–191.

Provensal, M., Mathis, C., Boyer, L., 1987. Bénard-von Kármán instability. Journal of Fluid Mechanics 182, 1–22.

Sahin, M., Owens, R.G., 2004. A numerical investigation of wall effects up to high blockage ratios on two-dimensional flow past a confined circular cylinder. Physics of Fluids 16, 1305–1320.

Sirovich, L., 1987. Turbulence and dynamics of coherent structures part 1: coherent structures. Quarterly of Applied Mathematics 45 (3), 561–571.

Sumer, B.M., Jensen, B.L., Fredsoe, J., 1991. Effect of a plane boundary on oscillatory flow around a circular cylinder. Journal of Fluid Mechanics 225, 271–300.

Van Oudheusden, B.W., Scarano, F., Van Hinsberg, N.P., Watt, D.W., 2005. Phase-resolved characterization of vortex shedding in the near wake of a square-section cylinder at incidence. Experiments in Fluids 39, 86–98.

Williamson, C.H.K., 1992. The natural and forced formation of spot-like vortex dislocations in the transition of a wake. Journal of Fluid Mechanics 243, 393–441.

Williamson, C.H.K., 1996. Vortex dynamics in the cylinder wake. Annual Review of Fluid Mechanics 28, 477–539.

Zdravkovich, M.M., 1997. Flow Around Circular Cylinders. vol. 1, Oxford University Press.

Zdravkovich, M.M., 2003. Flow Around Circular Cylinders: A Comprehensive Guide Through Flow Phenomena, Experiments, Applications, Mathematical Models, and Computer Simulations. vol. 2, Oxford University Press.

Zovatto, L., Pedrizzetti, G., 2001. Flow about a circular cylinder between parallel walls. Journal of Fluid Mechanics 440, 1–25.